Title

Study of the reactions e+e-→π+π-π0π0π0π0 and π+π-π0π0π0η at center-of-mass energies from threshold to 4.5 GeV using initial-state radiation

Journal

Physical Review D, 104(11)

ISSN

2470-0010

Authors

Lees, JP
Poireau, V
Tisserand, V
et al.

Publication Date

2021-12-01

DOI

10.1103/physrevd.104.112004

Peer reviewed

Study of the reactions $e^+e^- \to \pi^+\pi^-\pi^0\pi^0\pi^0\pi^0$ and $\pi^+\pi^-\pi^0\pi^0\pi^0\eta$ at center-of-mass energies from threshold to 4.5 GeV using initial-state radiation

J. P. Lees,[1] V. Poireau,[1] V. Tisserand,[1] E. Grauges,[2] A. Palano,[3] G. Eigen,[4] D. N. Brown,[5] Yu. G. Kolomensky,[5] M. Fritsch,[6] H. Koch,[6] T. Schroeder,[6] R. Cheaib,[7b] C. Hearty,[7a,7b] T. S. Mattison,[7b] J. A. McKenna,[7b] R. Y. So,[7b] V. E. Blinov,[8a,8b,8c] A. R. Buzykaev,[8a] V. P. Druzhinin,[8a,8b] V. B. Golubev,[8a,8b] E. A. Kozyrev,[8a,8b] E. A. Kravchenko,[8a,8b] A. P. Onuchin,[8a,8b,8c,*] S. I. Serednyakov,[8a,8b] Yu. I. Skovpen,[8a,8b] E. P. Solodov,[8a,8b] K. Yu. Todyshev,[8a,8b] A. J. Lankford,[9] B. Dey,[10] J. W. Gary,[10] O. Long,[10] A. M. Eisner,[11] W. S. Lockman,[11] W. Panduro Vazquez,[11] D. S. Chao,[12] C. H. Cheng,[12] B. Echenard,[12] K. T. Flood,[12] D. G. Hitlin,[12] J. Kim,[12] Y. Li,[12] D. X. Lin,[12] S. Middleton,[12] T. S. Miyashita,[12] P. Ongmongkolkul,[12] J. Oyang,[12] F. C. Porter,[12] M. Röhrken,[12] Z. Huard,[13] B. T. Meadows,[13] B. G. Pushpawela,[13] M. D. Sokoloff,[13] L. Sun,[13,†] J. G. Smith,[14] S. R. Wagner,[14] D. Bernard,[15] M. Verderi,[15] D. Bettoni,[16a] C. Bozzi,[16a] R. Calabrese,[16a,16b] G. Cibinetto,[16a,16b] E. Fioravanti,[16a,16b] I. Garzia,[16a,16b] E. Luppi,[16a,16b] V. Santoro,[16a] A. Calcaterra,[17] R. de Sangro,[17] G. Finocchiaro,[17] S. Martellotti,[17] P. Patteri,[17] I. M. Peruzzi,[17] M. Piccolo,[17] M. Rotondo,[17] A. Zallo,[17] S. Passaggio,[18] C. Patrignani,[18,‡] B. J. Shuve,[19] H. M. Lacker,[20] B. Bhuyan,[21] U. Mallik,[22] C. Chen,[23] J. Cochran,[23] S. Prell,[23] A. V. Gritsan,[24] N. Arnaud,[25] M. Davier,[25] F. Le Diberder,[25] A. M. Lutz,[25] G. Wormser,[25] D. J. Lange,[26] D. M. Wright,[26] J. P. Coleman,[27] E. Gabathuler,[27,*] D. E. Hutchcroft,[27] D. J. Payne,[27] C. Touramanis,[27] A. J. Bevan,[28] F. Di Lodovico,[28,§] R. Sacco,[28] G. Cowan,[29] Sw. Banerjee,[30] D. N. Brown,[30,‖] C. L. Davis,[30] A. G. Denig,[31] W. Gradl,[31] K. Griessinger,[31] A. Hafner,[31] K. R. Schubert,[31] R. J. Barlow,[32,¶] G. D. Lafferty,[32] R. Cenci,[33] A. Jawahery,[33] D. A. Roberts,[33] R. Cowan,[34] S. H. Robertson,[35a,35b] R. M. Seddon,[35b] N. Neri,[36a] F. Palombo,[36a,36b] L. Cremaldi,[37] R. Godang,[37,**] D. J. Summers,[37,*] P. Taras,[38] G. De Nardo,[39] C. Sciacca,[39] G. Raven,[40] C. P. Jessop,[41] J. M. LoSecco,[41] K. Honscheid,[42] R. Kass,[42] A. Gaz,[43a] M. Margoni,[43a,43b] M. Posocco,[43a] G. Simi,[43a,43b] F. Simonetto,[43a,43b] R. Stroili,[43a,43b] S. Akar,[44] E. Ben-Haim,[44] M. Bomben,[44] G. R. Bonneaud,[44] G. Calderini,[44] J. Chauveau,[44] G. Marchiori,[44] J. Ocariz,[44] M. Biasini,[45a,45b] E. Manoni,[45a] A. Rossi,[45a] G. Batignani,[46a,46b] S. Bettarini,[46a,46b] M. Carpinelli,[46a,46b,††] G. Casarosa,[46a,46b] M. Chrzaszcz,[46a] F. Forti,[46a,46b] M. A. Giorgi,[46a,46b] A. Lusiani,[46a,46c] B. Oberhof,[46a,46b] E. Paoloni,[46a,46b] M. Rama,[46a] G. Rizzo,[46a,46b] J. J. Walsh,[46a] L. Zani,[46a,46b] A. J. S. Smith,[47] F. Anulli,[48a] R. Faccini,[48a,48b] F. Ferrarotto,[48a] F. Ferroni,[48a,‡‡] A. Pilloni,[48a,48b] G. Piredda,[48a,*] C. Bünger,[49] S. Dittrich,[49] O. Grünberg,[49] M. Heß,[49] T. Leddig,[49] C. Voß,[49] R. Waldi,[49] T. Adye,[50] F. F. Wilson,[50] S. Emery,[51] G. Vasseur,[51] D. Aston,[52] C. Cartaro,[52] M. R. Convery,[52] J. Dorfan,[52] W. Dunwoodie,[52] M. Ebert,[52] R. C. Field,[52] B. G. Fulsom,[52] M. T. Graham,[52] C. Hast,[52] W. R. Innes,[52,*] P. Kim,[52] D. W. G. S. Leith,[52,*] S. Luitz,[52] D. B. MacFarlane,[52] D. R. Muller,[52] H. Neal,[52] B. N. Ratcliff,[52] A. Roodman,[52] M. K. Sullivan,[52] J. Va'vra,[52] W. J. Wisniewski,[52] M. V. Purohit,[53] J. R. Wilson,[53] A. Randle-Conde,[54] S. J. Sekula,[54] H. Ahmed,[55] N. Tasneem,[55] M. Bellis,[56] P. R. Burchat,[56] E. M. T. Puccio,[56] M. S. Alam,[57] J. A. Ernst,[57] R. Gorodeisky,[58] N. Guttman,[58] D. R. Peimer,[58] A. Soffer,[58] S. M. Spanier,[59] J. L. Ritchie,[60] R. F. Schwitters,[60] J. M. Izen,[61] X. C. Lou,[61] F. Bianchi,[62a,62b] F. De Mori,[62a,62b] A. Filippi,[62a] D. Gamba,[62a,62b] L. Lanceri,[63] L. Vitale,[63] F. Martinez-Vidal,[64] A. Oyanguren,[64] J. Albert,[65b] A. Beaulieu,[65b] F. U. Bernlochner,[65b] G. J. King,[65b] R. Kowalewski,[65b] T. Lueck,[65b] C. Miller,[65b] I. M. Nugent,[65b] J. M. Roney,[65b] R. J. Sobie,[65a,65b] T. J. Gershon,[66] P. F. Harrison,[66] T. E. Latham,[66] R. Prepost,[67] and S. L. Wu[67]

[1]*Laboratoire d'Annecy-le-Vieux de Physique des Particules (LAPP), Université de Savoie, CNRS/IN2P3, F-74941 Annecy-Le-Vieux, France*
[2]*Departament ECM, Facultat de Fisica, Universitat de Barcelona, E-08028 Barcelona, Spain*
[3]*INFN Sezione di Bari, I-70126 Bari, Italy*
[4]*Institute of Physics, University of Bergen, N-5007 Bergen, Norway*
[5]*Lawrence Berkeley National Laboratory and University of California, Berkeley, California 94720, USA*
[6]*Institut für Experimentalphysik 1, Ruhr Universität Bochum, D-44780 Bochum, Germany*
[7a]*Institute of Particle Physics, Vancouver, British Columbia V6T 1Z1, Canada*
[7b]*University of British Columbia, Vancouver, British Columbia, Canada V6T 1Z1*
[8a]*Budker Institute of Nuclear Physics SB RAS, Novosibirsk 630090, Russia*
[8b]*Novosibirsk State University, Novosibirsk 630090, Russia*
[8c]*Novosibirsk State Technical University, Novosibirsk 630092, Russia*
[9]*University of California at Irvine, Irvine, California 92697, USA*
[10]*University of California at Riverside, Riverside, California 92521, USA*
[11]*Institute for Particle Physics, University of California at Santa Cruz, Santa Cruz, California 95064, USA*
[12]*California Institute of Technology, Pasadena, California 91125, USA*
[13]*University of Cincinnati, Cincinnati, Ohio 45221, USA*
[14]*University of Colorado, Boulder, Colorado 80309, USA*

[15]*Laboratoire Leprince-Ringuet, Ecole Polytechnique, CNRS/IN2P3, F-91128 Palaiseau, France*
[16a]*INFN Sezione di Ferrara, I-44122 Ferrara, Italy*
[16b]*Dipartimento di Fisica e Scienze della Terra, Università di Ferrara, I-44122 Ferrara, Italy*
[17]*INFN Laboratori Nazionali di Frascati, I-00044 Frascati, Italy*
[18]*INFN Sezione di Genova, I-16146 Genova, Italy*
[19]*Harvey Mudd College, Claremont, California 91711, USA*
[20]*Institut für Physik, Humboldt-Universität zu Berlin, D-12489 Berlin, Germany*
[21]*Indian Institute of Technology Guwahati, Guwahati, Assam, 781 039, India*
[22]*University of Iowa, Iowa City, Iowa 52242, USA*
[23]*Iowa State University, Ames, Iowa 50011, USA*
[24]*Johns Hopkins University, Baltimore, Maryland 21218, USA*
[25]*CNRS/IN2P3, IJCLab, Université Paris-Saclay, F-91405 Orsay, France*
[26]*Lawrence Livermore National Laboratory, Livermore, California 94550, USA*
[27]*University of Liverpool, Liverpool L69 7ZE, United Kingdom*
[28]*Queen Mary, University of London, London E1 4NS, United Kingdom*
[29]*University of London, Royal Holloway and Bedford New College, Egham, Surrey TW20 0EX, United Kingdom*
[30]*University of Louisville, Louisville, Kentucky 40292, USA*
[31]*Institut für Kernphysik, Johannes Gutenberg-Universität Mainz, D-55099 Mainz, Germany*
[32]*University of Manchester, Manchester M13 9PL, United Kingdom*
[33]*University of Maryland, College Park, Maryland 20742, USA*
[34]*Laboratory for Nuclear Science, Massachusetts Institute of Technology, Cambridge, Massachusetts 02139, USA*
[35a]*Institute of Particle Physics, Montréal, Québec H3A 2T8, Canada*
[35b]*McGill University, Montréal, Québec H3A 2T8, Canada*
[36a]*INFN Sezione di Milano, I-20133 Milano, Italy*
[36b]*Dipartimento di Fisica, Università di Milano, I-20133 Milano, Italy*
[37]*University of Mississippi, University, Mississippi 38677, USA*
[38]*Physique des Particules, Université de Montréal, Montréal, Québec H3C 3J7, Canada*
[39]*INFN Sezione di Napoli and Dipartimento di Scienze Fisiche, Università di Napoli Federico II, I-80126 Napoli, Italy*
[40]*NIKHEF, National Institute for Nuclear Physics and High Energy Physics, NL-1009 DB Amsterdam, Netherlands*
[41]*University of Notre Dame, Notre Dame, Indiana 46556, USA*
[42]*Ohio State University, Columbus, Ohio 43210, USA*
[43a]*INFN Sezione di Padova, I-35131 Padova, Italy*
[43b]*Dipartimento di Fisica, Università di Padova, I-35131 Padova, Italy*
[44]*Laboratoire de Physique Nucléaire et de Hautes Energies, Sorbonne Université, Paris Diderot Sorbonne Paris Cité, CNRS/IN2P3, F-75252 Paris, France*
[45a]*INFN Sezione di Perugia, I-06123 Perugia, Italy*
[45b]*Dipartimento di Fisica, Università di Perugia, I-06123 Perugia, Italy*
[46a]*INFN Sezione di Pisa, I-56127 Pisa, Italy*
[46b]*Dipartimento di Fisica, Università di Pisa, I-56127 Pisa, Italy*
[46c]*Scuola Normale Superiore di Pisa, I-56127 Pisa, Italy*
[47]*Princeton University, Princeton, New Jersey 08544, USA*
[48a]*INFN Sezione di Roma, I-00185 Roma, Italy*
[48b]*Dipartimento di Fisica, Università di Roma La Sapienza, I-00185 Roma, Italy*
[49]*Universität Rostock, D-18051 Rostock, Germany*
[50]*Rutherford Appleton Laboratory, Chilton, Didcot, Oxon OX11 0QX, United Kingdom*
[51]*IRFU, CEA, Université Paris-Saclay, F-91191 Gif-sur-Yvette, France*
[52]*SLAC National Accelerator Laboratory, Stanford, California 94309, USA*
[53]*University of South Carolina, Columbia, South Carolina 29208, USA*
[54]*Southern Methodist University, Dallas, Texas 75275, USA*
[55]*St. Francis Xavier University, Antigonish, Nova Scotia B2G 2W5, Canada*
[56]*Stanford University, Stanford, California 94305, USA*
[57]*State University of New York, Albany, New York 12222, USA*
[58]*School of Physics and Astronomy, Tel Aviv University, Tel Aviv 69978, Israel*
[59]*University of Tennessee, Knoxville, Tennessee 37996, USA*
[60]*University of Texas at Austin, Austin, Texas 78712, USA*
[61]*University of Texas at Dallas, Richardson, Texas 75083, USA*

[62a]INFN Sezione di Torino, I-10125 Torino, Italy
[62b]Dipartimento di Fisica, Università di Torino, I-10125 Torino, Italy
[63]INFN Sezione di Trieste and Dipartimento di Fisica, Università di Trieste, I-34127 Trieste, Italy
[64]IFIC, Universitat de Valencia-CSIC, E-46071 Valencia, Spain
[65a]Institute of Particle Physics, Victoria, British Columbia V8W 3P6, Canada
[65b]University of Victoria, Victoria, British Columbia V8W 3P6, Canada
[66]Department of Physics, University of Warwick, Coventry CV4 7AL, United Kingdom
[67]University of Wisconsin, Madison, Wisconsin 53706, USA

(Received 4 October 2021; accepted 16 November 2021; published 14 December 2021)

We study the processes $e^+e^- \to \pi^+\pi^-\pi^0\pi^0\pi^0\pi^0\gamma$ and $\pi^+\pi^-\pi^0\pi^0\pi^0\eta\gamma$ in which an energetic photon is radiated from the initial state. The data were collected with the *BABAR* detector at the SLAC National Accelerator Laboratory. About 7300 and 870 events, respectively, are selected from a data sample corresponding to an integrated luminosity of 469 fb^{-1}. The invariant mass of the hadronic final state defines the effective e^+e^- center-of-mass energy. The center-of-mass energies range from threshold to 4.5 GeV. From the mass spectra, the first ever measurements of the $e^+e^- \to \pi^+\pi^-\pi^0\pi^0\pi^0\pi^0$ and the $e^+e^- \to \pi^+\pi^-\pi^0\pi^0\pi^0\eta$ cross sections are performed. The contributions from $\omega\pi^0\pi^0\pi^0$, $\eta\pi^+\pi^-\pi^0$, $\omega\eta$, and other intermediate states are presented. We observe the J/ψ and $\psi(2S)$ in most of these final states and measure the corresponding branching fractions, many of them for the first time.

DOI: 10.1103/PhysRevD.104.112004

I. INTRODUCTION

Many precision Standard Model (SM) predictions require the hadronic vacuum polarization (HVP) terms to be taken into account. At a relatively large momentum transfer, these terms are measured by studying the inclusive hadron production in e^+e^- annihilation and are relatively well calculated by perturbative quantum chromodynamics. However, in the energy region from the hadronic threshold to about 2 GeV, the inclusive hadronic cross section cannot be measured or calculated reliably, and a sum of exclusive states must be used. It is particularly important for the calculation of the muon anomalous magnetic moment $(g_\mu - 2)$, which is most sensitive to the low-energy region. Despite large datasets of e^+e^- cross sections, accumulated in the past years, and the studies performed [1,2], there still is a discrepancy between the SM calculation and the experimental value. With the latest result of the $(g_\mu - 2)$ experiment at Fermilab [3], this discrepancy increased to 4.2 sigma.

Electron-positron annihilation events with initial-state radiation (ISR) can be used to study processes over a wide range of energies below the nominal e^+e^- c.m. energy ($E_{\rm c.m.}$), as proposed in Ref. [4]. The possibility of exploiting ISR to make precise measurements of low-energy cross sections at high-luminosity ϕ and B factories is discussed in Refs. [5–7] and motivates the studies described in this paper. Not all accessible states have yet been measured; thus new measurements will improve the reliability of the HVP calculation. In addition, studies of ISR events at B factories are interesting in their own right, because they provide information on resonance spectroscopy for masses up to the charmonium region.

Studies of hadron (h) production in the ISR processes $e^+e^- \to h\gamma$ using data from the *BABAR* experiment at SLAC have been previously reported [8–22]. Initial-state radiation events with detection of the ISR photon are characterized by good reconstruction efficiency and by well-understood kinematics, demonstrated in the references given above. The *BABAR* detector performance (tracking, particle identification, π^0, K^0_S, and K^0_L reconstruction) is well suited to the study of ISR processes.

This paper reports on analyses of the $\pi^+\pi^-4\pi^0$ and $\pi^+\pi^-3\pi^0\eta$ final states produced in conjunction with an energetic photon, assumed to result from ISR. While *BABAR* data cover effective c.m. energies up to 10.58 GeV, this analysis is restricted to energies below 4.5 GeV because of backgrounds from $\Upsilon(4S)$ decays.

There are no previous measurements of the $e^+e^- \to \pi^+\pi^-4\pi^0$ and $e^+e^- \to \pi^+\pi^-3\pi^0\eta$ cross sections. The

[*]Deceased.
[†]Present address: Wuhan University, Wuhan 430072, China.
[‡]Present address: Università di Bologna and INFN Sezione di Bologna, I-47921 Rimini, Italy.
[§]Present address: King's College, London WC2R 2LS, United Kingdom.
[‖]Present address: Western Kentucky University, Bowling Green, Kentucky 42101, USA.
[¶]Present address: University of Huddersfield, Huddersfield HD1 3DH, United Kingdom.
[**]Present address: University of South Alabama, Mobile, Alabama 36688, USA.
[††]Also at Università di Sassari, I-07100 Sassari, Italy.
[‡‡]Also at Gran Sasso Science Institute, I-67100 LAquila, Italy.

six-pion cross sections have a sizable value below 2 GeV [11] and the two-charged plus four-neutral pion processes are currently included in the HVP calculation by assuming isospin relations [1]. The direct measurement of this channel can reduce the calculation uncertainty. It is also important to extract the contribution of the intermediate resonances, because the total cross section calculation depends on their decay rate to the measured final states. Below, we present the measurements of $e^+e^- \to \omega\pi^0\pi^0\pi^0$, $e^+e^- \to \eta\pi^+\pi^-\pi^0$, and $e^+e^- \to \omega\eta$ cross sections, with $\eta \to \pi^0\pi^0\pi^0$, that contribute to the $e^+e^- \to \pi^+\pi^-4\pi^0$ final state.

A clear J/ψ signal is observed for both the $\pi^+\pi^-4\pi^0$ and $\pi^+\pi^-3\pi^0\eta$ channels, and the corresponding J/ψ branching fractions are measured.

II. THE *BABAR* DETECTOR AND DATASET

The data used in this analysis were collected with the *BABAR* detector at the PEP-II2 asymmetric-energy e^+e^- storage ring. The total integrated luminosity used is 468.6 fb^{-1} [23], which includes data collected at the $\Upsilon(4S)$ resonance (424.7 fb^{-1}) and at a c.m. energy 40 MeV below this resonance (43.9 fb^{-1}).

The *BABAR* detector is described in detail elsewhere [24]. Charged particles are reconstructed using the *BABAR* tracking system, which comprises the silicon vertex tracker (SVT) and the drift chamber (DCH), both located inside a 1.5 T solenoid. Separation of pions and kaons is accomplished by means of the detector of internally reflected Cherenkov light and energy-loss measurements in the SVT and DCH. Photons and K^0_L mesons are detected in the electromagnetic calorimeter (EMC). Muon identification is provided by the instrumented flux return.

To evaluate the detector acceptance and efficiency, we have developed a special package of Monte Carlo (MC) simulation programs for radiative processes based on the approach of Czyż and Kühn [25]. Multiple collinear soft-photon emission from the initial e^+e^- state is implemented with the structure function technique [26,27], while additional photon radiation from final-state particles is simulated using the PHOTOS package [28]. The precision of the radiative simulation is such that it contributes less than 1% to the uncertainty in the measured hadronic cross sections.

We simulate $e^+e^- \to \pi^+\pi^-\pi^0\pi^0\pi^0\pi^0\gamma$ events assuming production through the $\omega(782)\eta$ intermediate channel, with decay of the ω to three pions and decay of the η to all its measured decay modes [29].

A sample of 460 000 simulated events is generated for the signal reaction and processed through the detector response simulation, based on the GEANT4 package [30]. These events are reconstructed using the same software chain as the data. Most of the experimental events contain additional soft photons due to machine background or interactions in the detector material. Variations in the detector and background conditions are included in the simulation.

For the purpose of background estimation, large samples of events from the main relevant ISR processes ($5\pi\gamma$, $\rho\eta\gamma$, $\pi^+\pi^-\pi^0\pi^0\gamma$, etc.) are simulated. To evaluate the background from the relevant non-ISR processes, namely $e^+e^- \to q\bar{q}$ ($q = u$, d, s) and $e^+e^- \to \tau^+\tau^-$, simulated samples with integrated luminosities about that of the data are generated using the JETSET [31] and KORALB [32] programs, respectively. The cross sections for the above processes are known with an accuracy slightly better than 10%, which is sufficient for the present purposes.

III. EVENT SELECTION AND KINEMATIC FIT

A relatively clean sample of $\pi^+\pi^-4\pi^0\gamma$ and $\pi^+\pi^-3\pi^0\eta\gamma$ events is selected by requiring that there be two tracks reconstructed in the DCH, SVT, or both, and nine or more photons (sometimes up to 20), with an energy above 0.02 GeV in the EMC. We assume the photon with the highest energy to be the ISR photon, and we require its c.m. energy to be larger than 3 GeV.

We allow either two or three tracks in an event, with exactly one opposite-sign pair that extrapolates within 0.25 cm of the beam axis and 3.0 cm of the nominal collision point along that axis. The reason a third track is allowed is to capture a relatively small fraction of signal events that contain a background track. The two tracks that satisfy the extrapolation criteria are fit to a vertex, which is used as the point of origin in the calculation of the photon directions.

We subject each candidate event to a set of constrained kinematic fits and use the fit results, along with charged-particle identification, to select the final states of interest and evaluate backgrounds from other processes. The kinematic fits make use of the four-momenta and covariance matrices of the initial e^+, e^-, and the set of selected tracks and photons. The fitted three-momenta of each track and photon are then used in further calculations.

Excluding the photon with the highest c.m. energy, which is assumed to arise from ISR, we consider all independent sets of eight other photons and combine them into four pairs. For each set of eight photons, we test all possible independent combinations of four photon pairs. We consider those combinations in which the diphoton mass of at least three pairs lies within ± 35 MeV/c^2 ($\pm 3\sigma$ of the resolution) of the π^0 mass m_{π^0} [29]. The selected combinations are subjected to a fit in which the diphoton masses of the three pairs with $|m(\gamma\gamma) - m_{\pi^0}| < 35$ MeV/c^2 are constrained to m_{π^0}. For the signal hypothesis $e^+e^- \to \pi^+\pi^-3\pi^0\gamma\gamma_{\rm ISR}$ with the constraints due to four-momentum conservation, there are thus seven constraints (7C) in the fit. The photons in the remaining ("fourth") pair are treated as being independent. If all four photon pairs in the combination satisfy $|m(\gamma\gamma) - m_{\pi^0}| < 35$ MeV/c^2, we rotate the

combinations, allowing each of the four diphoton pairs in turn to be the fourth pair, i.e., the pair without the m_{π^0} constraint. The combination with the smallest χ^2 is retained, along with the obtained ${\chi^2}_{2\pi 3\pi^0\gamma\gamma}$ (χ^2_{7C}) value and the fitted three-momenta of each track and photon.

The above procedure allows us not only to search for events with $\pi^0 \to \gamma\gamma$ in the fourth photon pair, but also for events with $\eta \to \gamma\gamma$.

Each retained event is also subjected to a 7C fit under the $e^+e^- \to \pi^+\pi^- 3\pi^0\gamma_{\rm ISR}$ background hypothesis, and the smallest ${\chi^2}_{2\pi 3\pi^0}$ value from all photon combinations is retained. The $\pi^+\pi^- 3\pi^0$ process has a comparable cross section to the $\pi^+\pi^- 4\pi^0$ signal process and can contribute to the background when two or more background photons are present.

IV. ADDITIONAL SELECTION CRITERIA

The results of the 7C fit to events with two tracks and at least nine photon candidates are used to perform the final selection of the six-pion and the five-pion plus eta sample. We require the tracks to lie within the fiducial region of the DCH (0.45–2.40 rad) and to be inconsistent with being a kaon or muon. The photon candidates are required to lie within the fiducial region of the EMC (0.35–2.40 rad) and to have an energy larger than 0.035 GeV. The latter improves the signal-to-background ratio. A requirement that there be no charged tracks within 1 rad of the ISR photon reduces the $\tau^+\tau^-$ background to a negligible level. A requirement that any extra photons in an event each have an energy below 0.7 GeV slightly reduces the multiphoton background.

Figure 1(a) shows the invariant mass $m(\gamma\gamma)$ of the fourth photon pair vs ${\chi^2}_{2\pi 3\pi^0\gamma\gamma}$. Clear π^0 and η peaks are visible at small χ^2 values. We require ${\chi^2}_{2\pi 3\pi^0\gamma\gamma} < 70$ to select the signal events and apply ${\chi^2}_{2\pi 3\pi^0} > 30$ condition if these events also satisfy the $2\pi 3\pi^0$ background hypothesis. This requirement reduces the contamination due to $2\pi 3\pi^0$ events from 30% to about 1%–2%, while reducing the signal efficiency by only 5%.

Figure 1(b) shows the $m(\gamma\gamma)$ distribution after the above requirements have been applied. The dip in this distribution at the π^0 mass value is a consequence of the kinematic fit constraint of the best three photon pairs to the π^0 mass. Also, because of this constraint, the fourth photon pair is sometimes formed from photon candidates that are less well measured.

Figure 2 shows the $m(\gamma\gamma)$ distribution vs the invariant mass $m(2\pi 3\pi^0\gamma\gamma)$ for events [Fig. 2(a)] in the signal region ${\chi^2}_{2\pi 3\pi^0\gamma\gamma} < 70$ and [Fig. 2(b)] in a control region defined by

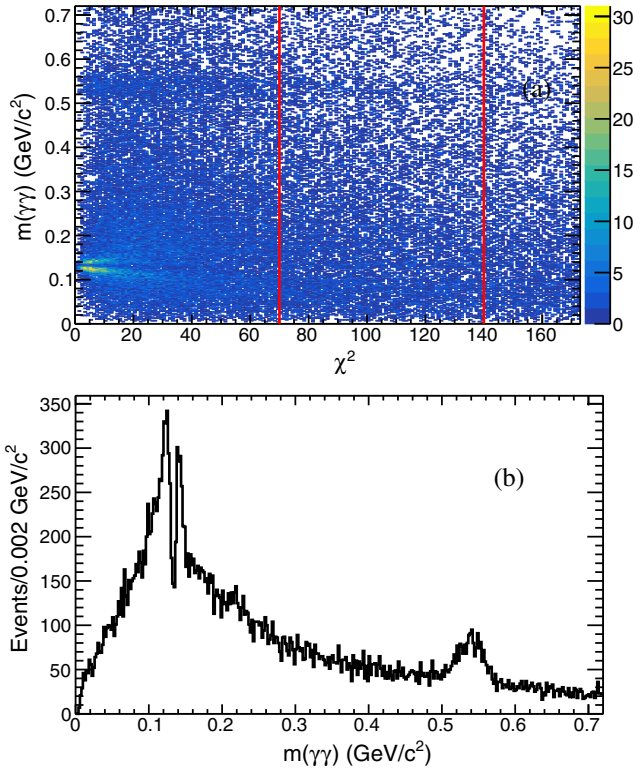

FIG. 1. (a) The invariant mass $m(\gamma\gamma)$ of the fourth photon pair vs ${\chi^2}_{2\pi 3\pi^0\gamma\gamma}$. (b) The $m(\gamma\gamma)$ distribution for ${\chi^2}_{2\pi 3\pi^0\gamma\gamma} < 70$ with additional selection criteria applied as described in the text. The double-peak structure near the π^0 mass is produced by the reconstruction procedure, as explained in the text.

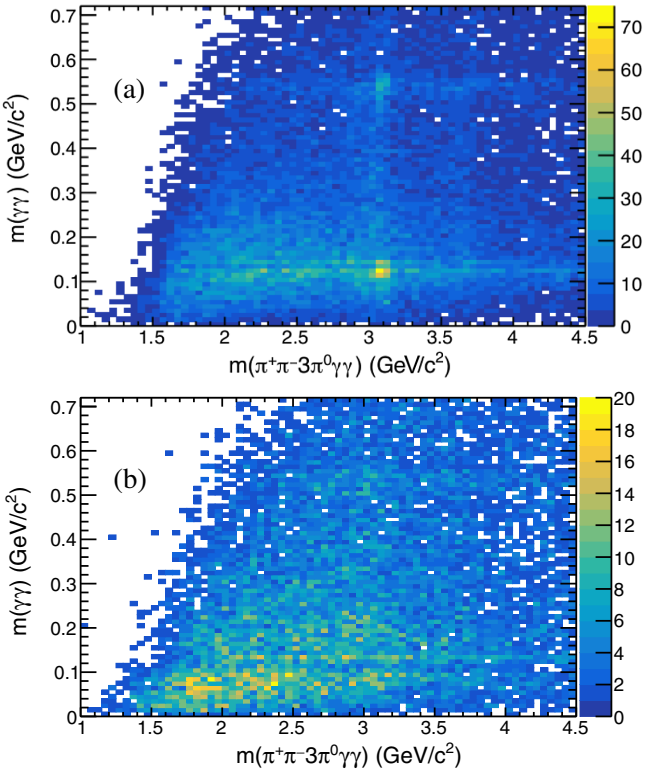

FIG. 2. (a) The fourth-photon-pair invariant mass $m(\gamma\gamma)$ vs $m(2\pi 3\pi^0\gamma\gamma)$ for (a) ${\chi^2}_{2\pi 3\pi^0\gamma\gamma} < 70$ and (b) $70 < {\chi^2}_{2\pi 3\pi^0\gamma\gamma} < 140$.

$70 < \chi^2_{2\pi 3\pi^0\gamma\gamma} < 140$. Events from the $e^+e^- \to \pi^+\pi^- 4\pi^0$ and $\pi^+\pi^- 3\pi^0\eta$ processes are clearly seen in the signal region, as well as J/ψ decays to these final states. No significant structures are seen in the control region, and we use these events to evaluate background.

Our strategy to extract the signals for the $e^+e^- \to \pi^+\pi^-\pi^0\pi^0\pi^0\pi^0$ and $\pi^+\pi^-\pi^0\pi^0\pi^0\eta$ processes is to perform a fit to the π^0 and η yields in intervals of 0.05 GeV/c^2 in the distribution of the invariant mass $m(\pi^+\pi^- 3\pi^0\gamma\gamma)$.

V. DETECTION EFFICIENCY

A. Number of signal events in simulation

As mentioned in Sec. II, the model used in the MC simulation assumes that the six-pion final state arises primarily through $\omega\eta$ production, with ω decays to three pions and η decays to $3\pi^0$. As shown below, events with η and ω dominate in the observed cross sections.

The selection procedure applied to the data is also applied to the MC-simulated events. Figure 3(a) shows the $m(\gamma\gamma)$ distribution for the χ^2 signal region and Fig. 3(b) shows the distribution of $m(\gamma\gamma)$ vs $m(2\pi 3\pi^0\gamma\gamma)$ for the simulated $\omega\eta$ events. The π^0 signal shape is not Gaussian due to the procedure explained in the previous section. It also includes a combinatoric background arising from the

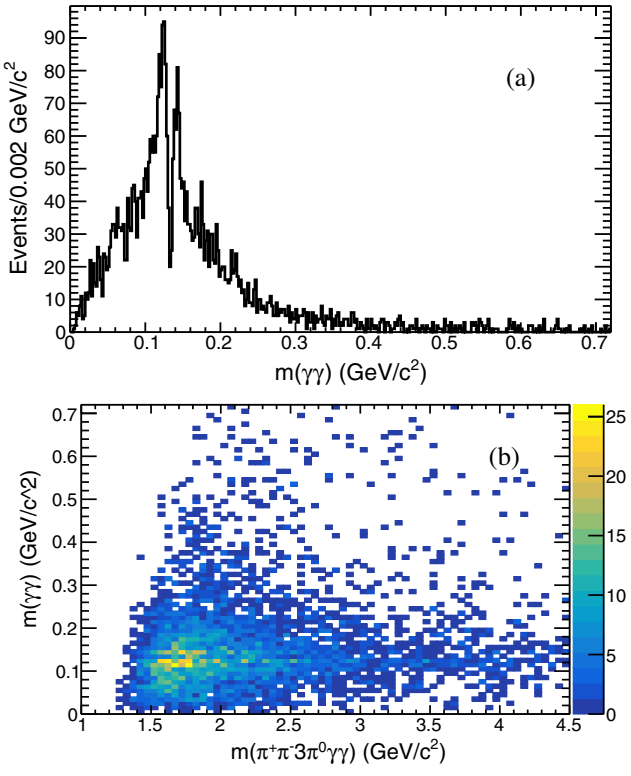

FIG. 3. The MC-simulated distribution for $e^+e^- \to \omega\eta$ events of (a) the fourth-photon-pair invariant mass $m(\gamma\gamma)$ and (b) $m(\gamma\gamma)$ vs $m(\pi^+\pi^- 3\pi^0\gamma\gamma)$.

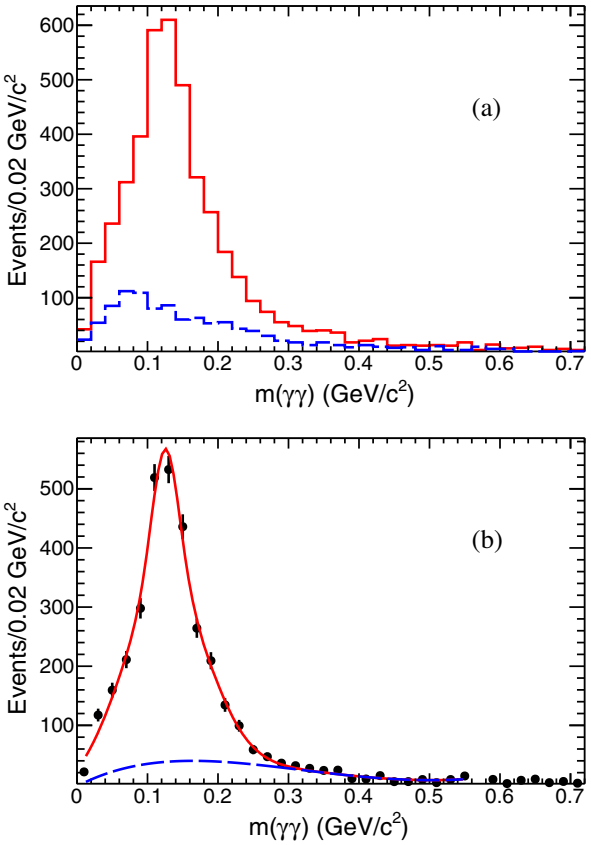

FIG. 4. The MC-simulated $m(\gamma\gamma)$ distribution for (a) $e^+e^- \to \omega\eta$ in the signal χ^2 region (solid histogram) and control region (dashed) and (b) background-subtracted $m(\gamma\gamma)$ distribution. The fit function is described in the text. The dashed curve shows the remaining background contribution.

combination of background photons, included in the simulation, with the photons from the signal reactions.

This background is subtracted as illustrated in Fig. 4, which shows the simulated $m(\gamma\gamma)$ distribution from Fig. 3(a) with a bin width of 0.02 GeV/c^2. The solid histogram in Fig. 4(a) corresponds to the two-photon mass distribution obtained from the χ^2 signal region. The dashed histogram is obtained instead from the control region and represents a combinatoric background distribution, which is subtracted assuming a scale factor that is varied to estimate the uncertainty in its contribution. The signal yield is then extracted by fitting the π^0 peak of this distribution with a sum of three Gaussian functions for the signal plus a second-order polynomial function to account for a residual combinatoric background. If a scale factor 1.5 is used, the background level becomes negligible, and we can determine and fix parameters for the signal function. If then we change the scale factor to 1.0 or to 0.0 in the fit, the obtained signal yield does not change by more than 3%. The result, for a scale factor of 1.0, is shown by the points in Fig. 4(b). The fit is shown by the smooth solid curve, while the dashed curve shows the contribution of the

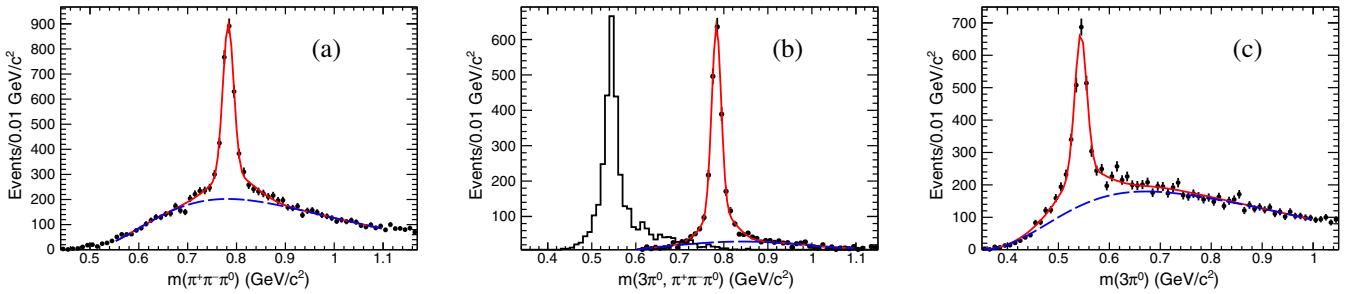

FIG. 5. The MC-simulated $e^+e^- \to \omega\eta$ events. (a) The $\pi^+\pi^-\pi^0$ invariant mass (four entries/event) with BW fit function (solid curve). The dashed curve shows the combinatoric background. (b) The $\pi^0\pi^0\pi^0$ invariant mass combination closest to the η mass (histogram) and the remaining $\pi^+\pi^-\pi^0$ invariant mass distribution (dots). The solid curve shows the ω signal fit and the dashed curve shows the remaining background. (c) The $\pi^0\pi^0\pi^0$ invariant mass for all selected MC-simulated events (four entries/event) with the fit functions used to determine the η signal.

remaining combinatoric background. The fitted signal yields 2639 ± 66 events. We apply a similar fit procedure in each 0.05 GeV/c^2 interval of the $m(\pi^+\pi^-3\pi^0\gamma\gamma)$ invariant mass distribution.

Alternatively, for $\omega\eta$ events, the ω mass peak can be used. Figure 5(a) shows the $\pi^+\pi^-\pi^0$ invariant mass (four entries per event) for selected MC-simulated events. A Breit-Wigner (BW) function, convolved with a Gaussian distribution to account for the detector resolution, is used to describe the ω signal. A second-order polynomial is used to describe the background. We obtain 2699 ± 75 events in total. We also obtain the number of events by fitting $m(\pi^+\pi^-\pi^0)$ in 0.05 GeV/c^2 intervals of the $m(\pi^+\pi^-3\pi^0\gamma\gamma)$ invariant mass.

Because in our simulation the ω and η mesons are produced in correlation, we can significantly reduce combinatorial background by selecting only one (from four) combination, in which the $3\pi^0$ invariant mass is closest to the η mass. The distribution of $m(3\pi^0)$ for this combination is shown in Fig. 5(b) by the histogram. In the remaining $\pi^+\pi^-\pi^0$ combination the ω signal, shown by dots in Fig. 5(b), has much lower background, and the fit yields 2796 ± 76 events in total. The $\pi^+\pi^-3\pi^0\gamma\gamma$ mass distribution is obtained by similar fitting in each 0.05 GeV/c^2 interval.

Similarly, as an alternative for the $\omega\eta$ events, we determine the number of events by fitting the η signal from the $\eta \to \pi^0\pi^0\pi^0$ decay: the simulated distribution is shown in Fig. 5(c) (four entries per event). The fit functions are the sum of three Gaussian functions and a polynomial for the combinatoric background. This fit yields 2569 ± 79 events in total. The $\pi^+\pi^-3\pi^0\gamma\gamma$ mass distribution is also obtained in each 0.05 GeV/c^2 interval.

B. Efficiency evaluation

The mass-dependent detection efficiency is obtained by dividing the number of fitted MC events in each 0.05 GeV/c^2 mass interval by the number generated in the same interval. By comparing the results of the four different methods, we conclude that the total efficiency does not change by more than 5% because of variations of the functions used to extract the number of events or the use of different background subtraction procedures. This value is taken as an estimate of the systematic uncertainty in the efficiency associated with the simulation model used and with the fit procedure. We average the four efficiencies in each 0.05 GeV/c^2 mass interval and fit the result with a third-order polynomial function, shown in Fig. 6. Although the signal simulation accounts for all η decay modes, the efficiency calculation considers only the $\eta \to \pi^0\pi^0\pi^0$ decay mode. From Fig. 6 it is seen that the reconstruction efficiency is about 2%, roughly independent of mass. The result of this fit is used for the cross section calculation.

This efficiency estimate takes into account the geometrical acceptance of the detector for the final-state photons and the charged pions, the inefficiency of the detector subsystems, and the event loss due to additional soft-photon emission from the initial and final states.

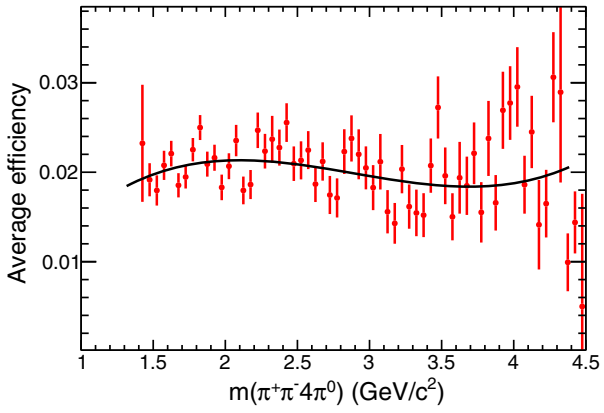

FIG. 6. The energy-dependent reconstruction efficiency for the $e^+e^- \to \pi^+\pi^-\pi^0\pi^0\pi^0\pi^0$ events. The curve shows the fit result, which is used in the cross section calculation.

Corrections to the efficiency that account for data-MC differences are discussed below.

VI. THE $\pi^+\pi^-4\pi^0$ FINAL STATE

A. Number of $\pi^+\pi^-4\pi^0$ events

The solid histogram in Fig. 7(a) shows the $m(\gamma\gamma)$ data of Fig. 1(b) binned in mass intervals of 0.02 GeV/c^2. The dashed histogram shows the distribution of data from the χ^2 control region. The dotted histogram is the estimated remaining background from the $e^+e^- \to \pi^+\pi^-3\pi^0$ process. No evidence for a peaking background is seen below 0.45 GeV/c^2 in either of the two background distributions. We subtract the background evaluated using the χ^2 control region with the scale factor 1.0. The resulting $m(\gamma\gamma)$ distribution is shown in Fig. 7(b).

We fit the data of Fig. 7(b) with a combination of a signal function, taken from a fit to simulated data, and a background function, taken to be a third-order polynomial. The fit is performed in the $m(\gamma\gamma)$ mass range from 0.0 to 0.45 GeV/c^2. The result of the fit is shown by the solid and dashed curves in Fig. 7(b). In total 7306 ± 164 events are obtained. Note that this number includes a relatively small peaking background component, due to $q\bar{q}$ events, which is discussed in Sec. VI B. The same fit is applied to the corresponding $m(\gamma\gamma)$ distribution in each 0.05 GeV/c^2 interval in the $\pi^+\pi^-3\pi^0\gamma\gamma$ invariant mass. The resulting number of $\pi^+\pi^-4\pi^0$ event candidates as a function of $m(\pi^+\pi^-4\pi^0)$, including the peaking $q\bar{q}$ background, is shown by the data points in Fig. 8.

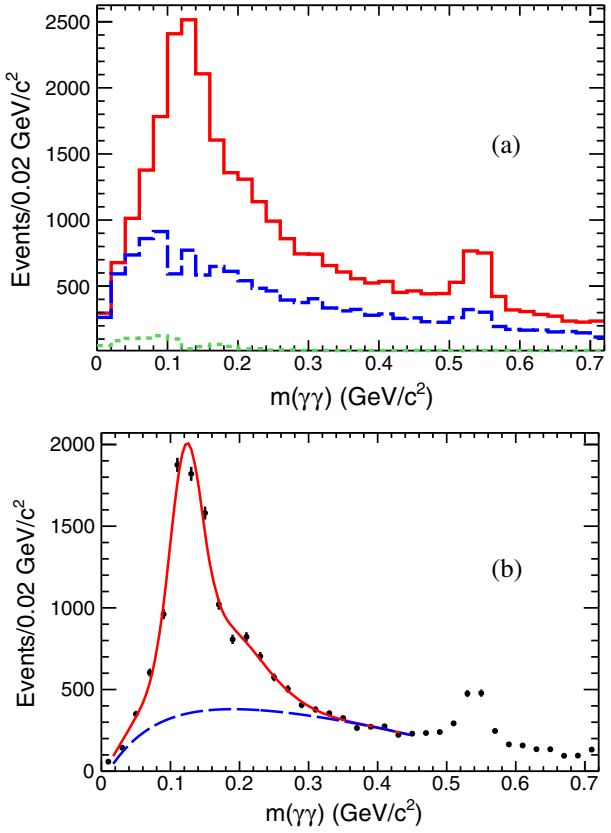

FIG. 7. (a) The fourth-photon-pair invariant mass $m(\gamma\gamma)$ for data in the signal (solid) and χ^2 control (dashed) regions. The dotted histogram shows the estimated remaining background in the signal region from $e^+e^- \to \pi^+\pi^-3\pi^0$. (b) The $m(\gamma\gamma)$ invariant mass for data after background subtraction. The curves are the fit results as described in the text.

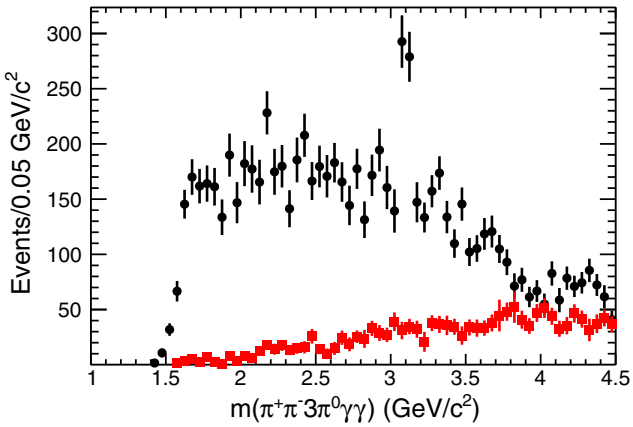

FIG. 8. The invariant mass distribution of $\pi^+\pi^-4\pi^0$ events (black circles), obtained from the fit to the π^0 mass peak. The contribution from non-ISR *uds* background is shown by red squares.

B. Peaking background

The major background producing a π^0 peak following application of the selection criteria of Sec. IV A is from non-ISR $q\bar{q}$ events, the most important channel being $e^+e^- \to \pi^+\pi^-\pi^0\pi^0\pi^0\pi^0$ in which one of the neutral pions decays asymmetrically, yielding a high-energy

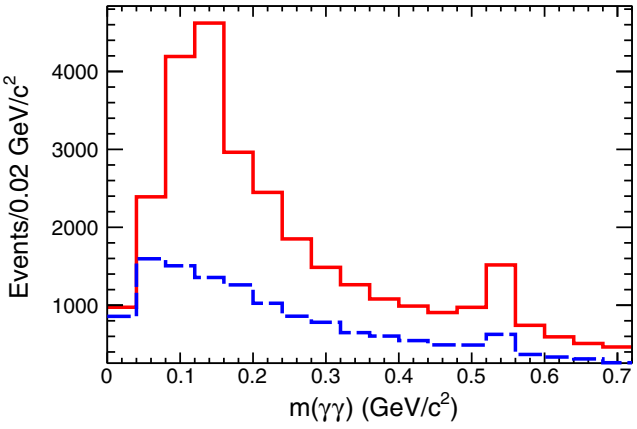

FIG. 9. The fourth-photon-pair invariant mass for the *uds* simulation for the signal region $\chi^2_{2\pi3\pi^0\gamma\gamma} < 70$ (solid histogram) and the control region $70 < \chi^2_{2\pi3\pi^0\gamma\gamma} < 140$ (dashed histogram).

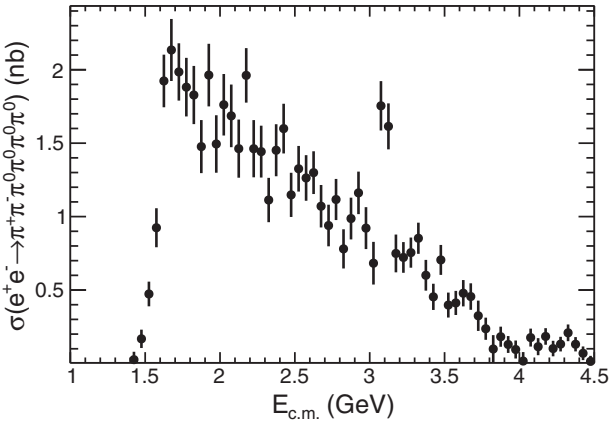

FIG. 10. The measured $e^+e^- \to \pi^+\pi^-\pi^0\pi^0\pi^0\pi^0$ cross section. The uncertainties are statistical only.

photon that mimics an ISR photon. We apply all our selection criteria and fit procedures to the non-ISR light quark $q\bar{q}$ (uds) simulation. Figure 9 shows the fourth-photon-pair invariant mass for $\chi^2_{2\pi 3\pi^0\gamma\gamma} < 70$ and $70 < \chi^2_{2\pi 3\pi^0\gamma\gamma} < 140$: clear signals from π^0 and η are seen.

To normalize the uds simulation, we form the diphoton invariant mass distribution of the ISR candidate with each of the other photons in the event. A π^0 peak is observed, with approximately the same number of events in data and simulation, leading to a normalization factor of 1.0 ± 0.1. The resulting uds background is shown in Fig. 8: the uds background is negligible below 2 GeV/c^2, but accounts for more than half the total spectrum for around 4 GeV/c^2 and above. We subtract this background for the cross section calculation.

C. Cross section for $e^+e^- \to \pi^+\pi^-\pi^0\pi^0\pi^0\pi^0$

The $e^+e^- \to \pi^+\pi^-\pi^0\pi^0\pi^0\pi^0$ Born cross section is determined from

$$\sigma(2\pi 4\pi^0)(E_{\rm c.m.}) = \frac{dN_{6\pi\gamma}(E_{\rm c.m.})}{d\mathcal{L}(E_{\rm c.m.})\epsilon_{6\pi}^{\rm corr}\epsilon_{6\pi}^{\rm MC}(E_{\rm c.m.})(1+\delta_R)}, \quad (1)$$

where $E_{\rm c.m.}$ is the invariant mass of the six-pion system; $dN_{6\pi\gamma}$ is the background-subtracted number of selected six-pion events in the interval $dE_{\rm c.m.}$, and $\epsilon_{6\pi}^{\rm MC}(E_{\rm c.m.})$ is the corresponding detection efficiency from simulation. The factor $\epsilon_{6\pi}^{\rm corr}$ accounts for the difference between data and simulation in the tracking ($1.0\% \pm 1.0\%$/per track) [10] and π^0 ($3.0\% \pm 1.0\%$ per pion) [19] reconstruction efficiencies. The ISR differential luminosity $d\mathcal{L}$ is calculated using the total integrated *BABAR* luminosity of 469 fb^{-1} [9]. The initial- and final-state soft-photon emission is accounted for by the radiative correction factor $(1+\delta_R)$, which is close to unity within a percent level for our selection criteria. The cross section results contain the effect of vacuum polarization because this effect is not accounted for in the luminosity calculation.

Our results for the $e^+e^- \to \pi^+\pi^-\pi^0\pi^0\pi^0\pi^0$ cross section are shown in Fig. 10. The cross section exhibits a structure around 1.7 GeV with a peak value of about 2 nb, followed by a monotonic decrease toward higher energies. Because we present our data in bins of width 0.050 GeV, compatible with the experimental resolution, we do not apply an unfolding procedure to the data. Numerical values for the cross section are presented in Table I. The J/ψ region is discussed later.

D. Summary of the systematic studies

The systematic uncertainties, presented in the previous sections, are summarized in Table II, along with the corrections that are applied to the measurements.

The three corrections applied to the cross sections sum up to 15.5%. The systematic uncertainties are estimated as 12.4%. The largest systematic uncertainty arises from the fitting and background subtraction procedures. This is

TABLE I. Summary of the $e^+e^- \to \pi^+\pi^-\pi^0\pi^0\pi^0\pi^0$ cross section measurement. The uncertainties are statistical only.

$E_{\rm c.m.}$ (GeV)	σ (nb)	$E_{\rm c.m.}$ (GeV)	σ (nb)	$E_{\rm c.m.}$ (GeV)	σ (nb)	$E_{\rm c.m.}$ (GeV)	σ (nb)	$E_{\rm c.m.}$ (GeV)	σ (nb)
1.425	0.03 ± 0.05	2.075	1.69 ± 0.21	2.725	0.94 ± 0.14	3.375	0.60 ± 0.10	4.025	0.02 ± 0.06
1.475	0.17 ± 0.06	2.125	1.46 ± 0.20	2.775	1.12 ± 0.14	3.425	0.45 ± 0.09	4.075	0.18 ± 0.06
1.525	0.47 ± 0.08	2.175	1.96 ± 0.19	2.825	0.78 ± 0.13	3.475	0.71 ± 0.10	4.125	0.11 ± 0.06
1.575	0.92 ± 0.13	2.225	1.46 ± 0.19	2.875	0.99 ± 0.14	3.525	0.40 ± 0.08	4.175	0.18 ± 0.06
1.625	1.92 ± 0.18	2.275	1.44 ± 0.18	2.925	1.16 ± 0.14	3.575	0.41 ± 0.08	4.225	0.10 ± 0.05
1.675	2.13 ± 0.21	2.325	1.11 ± 0.15	2.975	0.92 ± 0.14	3.625	0.48 ± 0.09	4.275	0.13 ± 0.05
1.725	1.99 ± 0.20	2.375	1.45 ± 0.18	3.025	0.68 ± 0.15	3.675	0.46 ± 0.09	4.325	0.21 ± 0.06
1.775	1.88 ± 0.20	2.425	1.60 ± 0.17	3.075	1.75 ± 0.17	3.725	0.32 ± 0.10	4.375	0.13 ± 0.05
1.825	1.83 ± 0.20	2.475	1.15 ± 0.15	3.125	1.61 ± 0.16	3.775	0.24 ± 0.08	4.425	0.07 ± 0.05
1.875	1.48 ± 0.18	2.525	1.33 ± 0.16	3.175	0.75 ± 0.13	3.825	0.10 ± 0.09	4.475	0.01 ± 0.04
1.925	1.96 ± 0.21	2.575	1.26 ± 0.16	3.225	0.72 ± 0.10	3.875	0.18 ± 0.07		
1.975	1.49 ± 0.20	2.625	1.30 ± 0.15	3.275	0.75 ± 0.10	3.925	0.13 ± 0.06		
2.025	1.76 ± 0.21	2.675	1.07 ± 0.14	3.325	0.85 ± 0.11	3.975	0.10 ± 0.06		

TABLE II. Summary of the systematic uncertainties in the $e^+e^- \to \pi^+\pi^-\pi^0\pi^0\pi^0\pi^0$ cross section measurement. The total uncertainly is computed assuming no correlations.

Source	Correction	Uncertainty
Luminosity	···	1%
MC-data difference in ISR photon efficiency	+1.5%	1%
χ^2 cut uncertainty	···	3%
Fit and background subtraction	···	10%
MC-data difference in track losses	+2%	1%
MC-data difference in π^0 losses	+12%	4%
Radiative corrections accuracy	···	1%
Efficiency from MC (model-fit-dependent)	···	5%
Total	+15.5%	12.4%

estimated by varying the background levels and the parameters of the functions used.

E. Overview of the intermediate structures

The $e^+e^- \to \pi^+\pi^-\pi^0\pi^0\pi^0\pi^0$ process has a rich internal substructure. To study this substructure, we impose the restriction $m(\gamma\gamma) < 0.35$ GeV/c^2, eliminating the region populated by $e^+e^- \to \pi^+\pi^-\pi^0\pi^0\pi^0\eta$, but with some level of the background remaining. We then assume that the $m(\pi^+\pi^-3\pi^0\gamma\gamma)$ invariant mass can be taken to represent $m(\pi^+\pi^-4\pi^0)$.

Figure 11(a) shows the distribution of the $\pi^0\pi^0\pi^0$ invariant mass (four entries per event). The distribution is seen to exhibit a prominent η peak, which is due to the $e^+e^- \to \eta\pi^+\pi^-\pi^0$ reaction. Figure 11(b) presents a scatter plot of the $\pi^0\pi^0\pi^0$ vs the $\pi^+\pi^-\pi^0$ invariant mass. From this plot, the $\omega\eta$ intermediate state is seen. Figure 11(c) presents a scatter plot of the $3\pi^0$ invariant mass versus $m(\pi^+\pi^-3\pi^0\gamma\gamma)$.

The distribution of the $\pi^+\pi^-\pi^0$ invariant mass (four entries per event) is shown in Fig. 12(a). A prominent ω peak from $e^+e^- \to \omega 3\pi^0$ is seen. The scatter plot in Fig. 12(b) shows $\pi^0\pi^0\pi^0$ vs the $\pi^+\pi^-\pi^0$ invariant mass for events from Fig. 11(b) when only the $3\pi^0$ combination with the invariant mass closest to the nominal η mass is kept. Correlated η and ω production is seen. A scatter plot of the $\pi^+\pi^-\pi^0$ vs the $\pi^+\pi^-3\pi^0\gamma\gamma$ mass is shown in Fig. 12(c). A clear signal for a J/ψ peak is also observed.

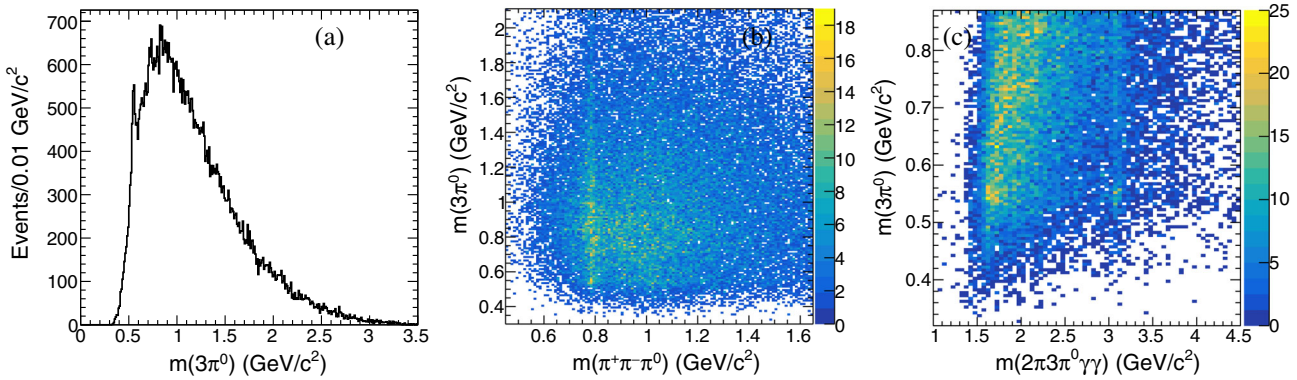

FIG. 11. (a) The $\pi^0\pi^0\pi^0$ invariant mass (four combinations per event). (b) The $\pi^0\pi^0\pi^0$ vs the $\pi^+\pi^-\pi^0$ invariant mass. (c) The $\pi^0\pi^0\pi^0$ invariant mass vs the six-pion invariant mass.

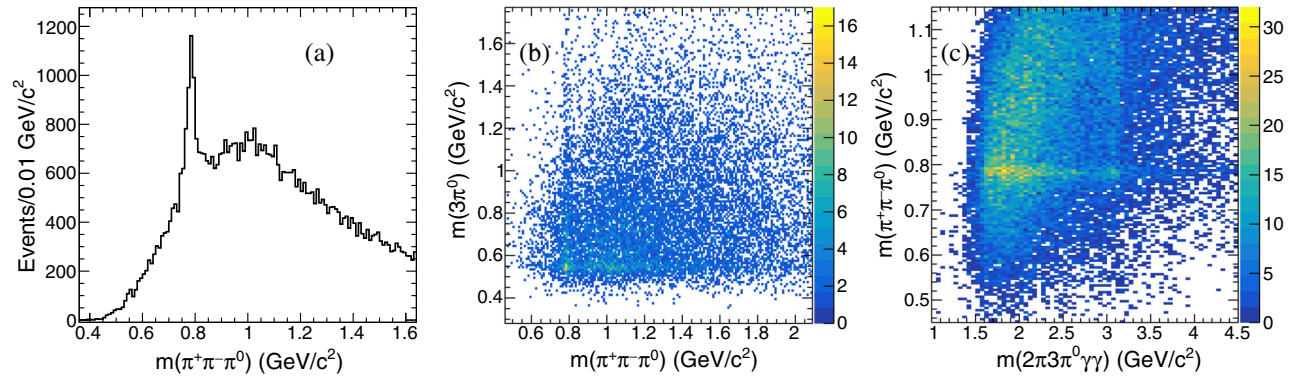

FIG. 12. (a) The $\pi^+\pi^-\pi^0$ invariant mass (four combinations per event). (b) The same as Fig. 11(b) but the $\pi^0\pi^0\pi^0$ invariant mass closest to the η mass is selected (one entry per event). (c) The $\pi^+\pi^-\pi^0$ invariant mass vs the six-pion invariant mass.

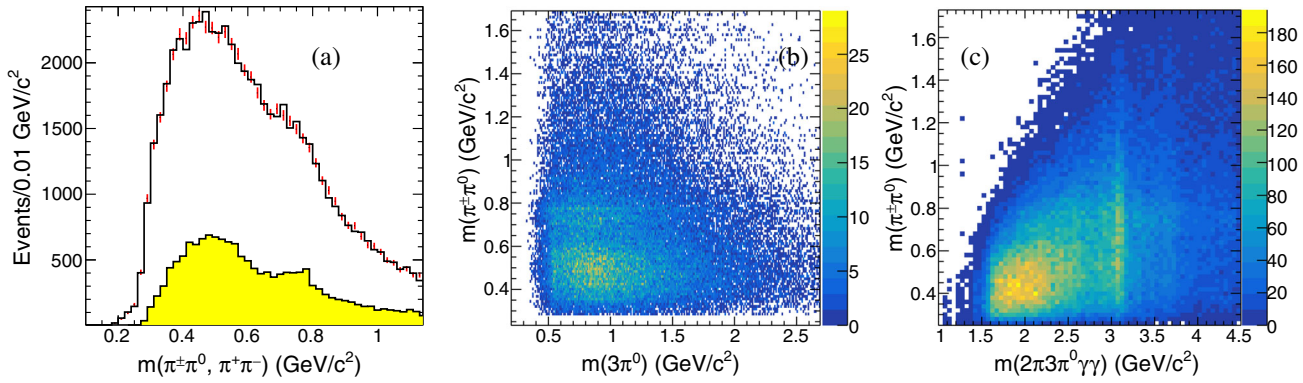

FIG. 13. (a) The $\pi^+\pi^-$ (shaded), $\pi^+\pi^0$ (solid), and $\pi^-\pi^0$ (points with errors) invariant masses (four combinations per event for ρ^+ and for ρ^-). (b) The $\pi^\pm\pi^0$ vs the $3\pi^0$ invariant mass (eight combinations per event). (c) The $\pi^\pm\pi^0$ invariant mass vs the six-pion invariant mass.

Figure 13(a) shows the $\pi^+\pi^0$(solid) and $\pi^-\pi^0$(points) invariant masses (four entries per event). Prominent $\rho(770)^\pm$ peaks, corresponding to $e^+e^- \to \rho^\pm\pi^\mp 3\pi^0$ (or $\rho^\pm\rho^\mp 2\pi^0$), are visible. The shaded histogram shows the presence of the ρ^0 signal. The scatter plot in Fig. 13(b) shows the $\pi^\pm\pi^0$ vs the $3\pi^0$ invariant mass. An indication of the $\rho^\pm\pi^\mp\eta$ (or $\rho^0\eta\pi^0$—not shown) intermediate state is visible. Figure 13(c) shows the $\pi^\pm\pi^0$ invariant mass vs the six-pion invariant mass: a clear signal for the J/ψ and an indication for the $\psi(2S)$ are seen.

F. The $\eta\pi^+\pi^-\pi^0$ intermediate state

To determine the contribution of the $\eta\pi^+\pi^-\pi^0$ intermediate state, we fit the events of Fig. 11(a) using a triple-Gaussian function to describe the signal peak, as in Fig. 5(c), and a polynomial to describe the background. The result of the fit is shown in Fig. 14. We obtain 1539 ± 89 $\eta\pi^+\pi^-\pi^0$ events. The number of $\eta\pi^+\pi^-\pi^0$ events as a function of the six-pion invariant mass is determined by performing an analogous fit to the events in Fig. 11(c) in each 0.05 GeV/c^2 interval of $m(\pi^+\pi^-4\pi^0)$. The resulting distribution is shown in Fig. 15 by triangles in comparison with all $\pi^+\pi^-4\pi^0$ events (dots).

Using Eq. (1), we determine the cross section for the $e^+e^- \to \eta\pi^+\pi^-\pi^0$ process. The results, which account for the $\eta \to 3\pi^0$ branching fractions of 0.327, are reported in Fig. 16 and Table III. Systematic uncertainties in this measurement are the same as those listed in Table II. Figure 16 shows our measurement in comparison to the SND result [33] and to those from the CMD-3 experiment [34]. These previous results are based on a different η decay mode from that considered here. The insert shows an expanded view for the c.m. energies below 2 GeV, where the resonance, interpreted as the $\omega(1650)$, dominates. The results of the three experiments are seen to agree within the uncertainties.

G. The $\eta\omega$ intermediate state

To determine the contribution of the $\eta\omega$ intermediate state to the $\eta\pi^+\pi^-\pi^0$ events, we select the $3\pi^0$ combination

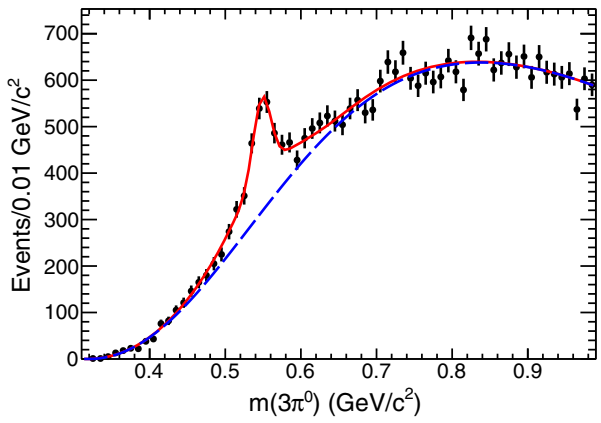

FIG. 14. The $3\pi^0$ invariant mass for data. The curves show the fit functions. The solid curve shows the η peak (based on MC simulation) plus the non-η continuum background (dashed).

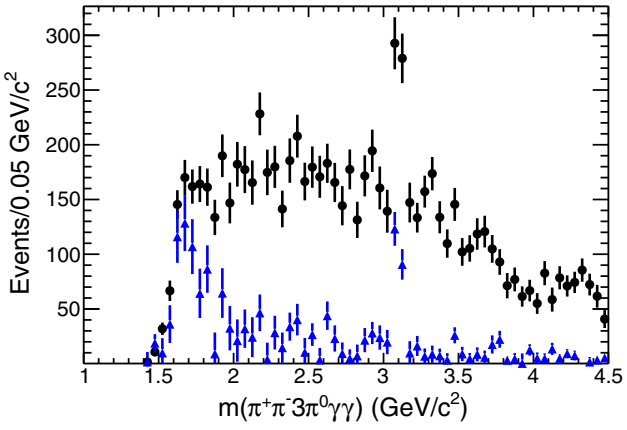

FIG. 15. The $m(\pi^+\pi^-4\pi^0)$ invariant mass dependence of the selected data events for $e^+e^- \to \eta\pi^+\pi^-\pi^0$, $\eta \to 3\pi^0$ (triangles) in comparison with all six-pion events (dots).

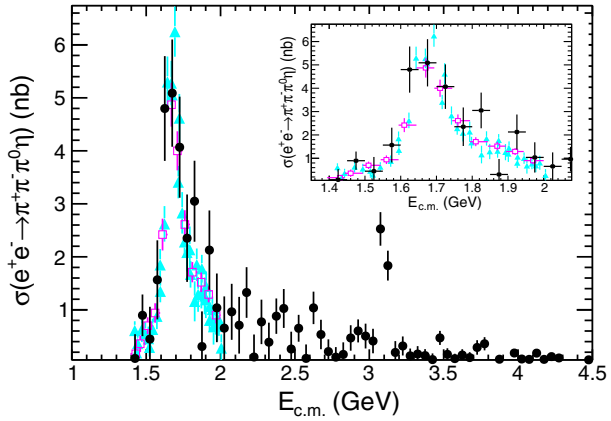

FIG. 16. Comparison of the current results (dots) for the $e^+e^- \to \pi^+\pi^-\pi^0\eta$ cross section with those from the SND experiment with $\eta \to \gamma\gamma$, shown by squares [33] and with those from the CMD-3 experiment, also based on $\eta \to \gamma\gamma$, shown by triangles [34]. The insert shows an expanded view of the resonant region.

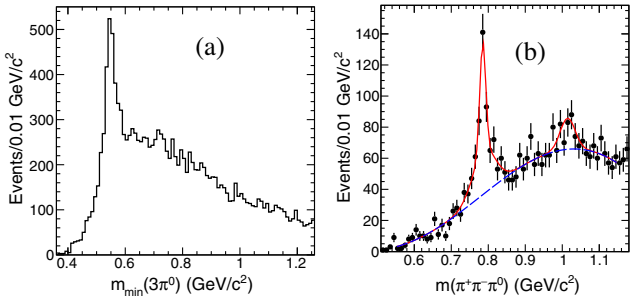

FIG. 17. (a) The $3\pi^0$ invariant mass closest to the η mass. (b) The $\pi^+\pi^-\pi^0$ invariant mass for events with $m_{\rm min}(3\pi^0) < 0.7$ GeV$/c^2$. The curves show the fit functions. The solid curve shows the ω and ϕ peak (based on MC simulation fit) plus the continuum background (dashed).

with the invariant mass closest to the nominal η mass, $m_{\rm min}(3\pi^0)$, and search for the ω signal in the remaining $\pi^+\pi^-\pi^0$ combination. Figure 17(a) shows the $m_{\rm min}(3\pi^0)$ distribution; Fig. 17(b) is the distribution for the corresponding $\pi^+\pi^-\pi^0$ invariant mass in the event. An additional requirement $m_{\rm min}(3\pi^0) < 0.7$ GeV$/c^2$ is applied. Prominent ω and ϕ peaks are seen. The latter arises from the $e^+e^- \to \eta\phi, \phi \to \pi^+\pi^-\pi^0$ reaction.

We fit the events of Fig. 17(b) using a double-Gaussian function to describe the signal from the ω and ϕ peaks, and a polynomial to describe the background. We obtain 351 ± 43 and 100 ± 32 $\eta\omega$ and $\eta\phi$ events, respectively. The number of $\eta\omega$ and $\eta\phi$ events as a function of the six-pion invariant mass is determined by performing an analogous fit to the events in each 0.05 GeV$/c^2$ interval of $m(\pi^+\pi^-4\pi^0)$. The resulting distributions are shown in Fig. 18.

Using Eq. (1), we determine the cross section for the $e^+e^- \to \eta\omega$ process. The results, accounting for the η branching fractions, are reported in Fig. 19 and listed in Table IV. Systematic uncertainties in this measurement are the same as those listed in Table II. Figure 19 shows our measurement in comparison to the *BABAR* result [11] (open circles), the SND result [33] (squares), and the CMD-3 result [34] (triangles). The insert shows an expanded view of the resonant region, where signal from the $\omega(1650)$ dominates. These previous results are based on different η decay modes ($\eta \to \pi^+\pi^-\pi^0$ for *BABAR*, $\eta \to \gamma\gamma$ for SND and CMD-3) from that considered here. The results from the different experiments are seen to agree within the uncertainties. Including the results of the present study, we have thus now measured the $e^+e^- \to \eta\omega$ cross section in two different η decay modes.

The observed contribution from the $e^+e^- \to \eta\phi$ reaction is small and we do not calculate its cross section.

H. The $\omega 3\pi^0$ intermediate state

To determine the contribution of the $\omega 3\pi^0$ intermediate state, we fit the events of Fig. 12(a) using a BW function

TABLE III. Summary of the $e^+e^- \to \eta\pi^+\pi^-\pi^0$ cross section measurement. The uncertainties are statistical only.

$E_{\rm c.m.}$ (GeV)	σ (nb)	$E_{\rm c.m.}$ (GeV)	σ (nb)	$E_{\rm c.m.}$ (GeV)	σ (nb)	$E_{\rm c.m.}$ (GeV)	σ (nb)	$E_{\rm c.m.}$ (GeV)	σ (nb)
1.425	0.08 ± 0.46	2.075	0.96 ± 0.53	2.725	0.21 ± 0.23	3.375	0.14 ± 0.12	4.025	0.07 ± 0.07
1.475	0.90 ± 0.39	2.125	0.71 ± 0.54	2.775	0.11 ± 0.19	3.425	0.06 ± 0.12	4.075	0.07 ± 0.07
1.525	0.45 ± 0.61	2.175	1.33 ± 0.48	2.825	0.16 ± 0.23	3.475	0.47 ± 0.13	4.125	0.18 ± 0.07
1.575	1.57 ± 0.75	2.225	0.11 ± 0.42	2.875	0.47 ± 0.24	3.525	0.16 ± 0.12	4.175	0.07 ± 0.05
1.625	4.80 ± 0.99	2.275	0.77 ± 0.42	2.925	0.60 ± 0.22	3.575	0.08 ± 0.09	4.225	0.12 ± 0.05
1.675	5.09 ± 1.01	2.325	0.39 ± 0.37	2.975	0.50 ± 0.23	3.625	0.15 ± 0.11	4.275	0.09 ± 0.05
1.725	4.07 ± 0.95	2.375	0.88 ± 0.33	3.025	0.41 ± 0.23	3.675	0.10 ± 0.10	4.325	0.00 ± 0.02
1.775	2.35 ± 0.82	2.425	1.03 ± 0.37	3.075	2.53 ± 0.32	3.725	0.29 ± 0.14	4.375	0.02 ± 0.05
1.825	3.05 ± 0.76	2.475	0.26 ± 0.33	3.125	1.83 ± 0.28	3.775	0.36 ± 0.12	4.425	0.04 ± 0.04
1.875	0.31 ± 0.66	2.525	0.65 ± 0.25	3.175	0.20 ± 0.21	3.825	0.05 ± 0.06	4.475	0.06 ± 0.04
1.925	2.13 ± 0.75	2.575	0.08 ± 0.26	3.225	0.32 ± 0.18	3.875	0.07 ± 0.08		
1.975	1.04 ± 0.65	2.625	1.04 ± 0.31	3.275	0.13 ± 0.14	3.925	0.00 ± 0.14		
2.025	0.65 ± 0.60	2.675	0.53 ± 0.28	3.325	0.17 ± 0.15	3.975	0.18 ± 0.08		

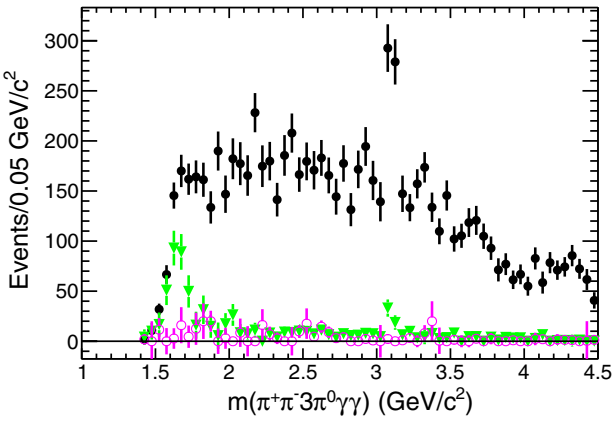

FIG. 18. The $m(\pi^+\pi^-4\pi^0)$ invariant mass dependence of the selected data events for $e^+e^- \to \eta\omega$, $\eta \to 3\pi^0$ (triangles) and $e^+e^- \to \eta\phi$, $\eta \to 3\pi^0$ (open circles) in comparison with all six-pion events (dots).

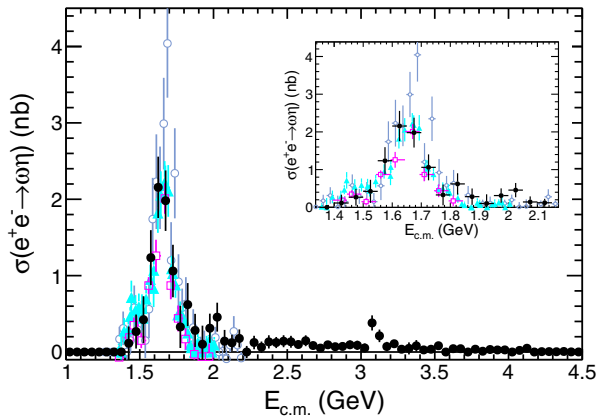

FIG. 19. Comparison of the current results (dots) for the $e^+e^- \to \eta\omega$ cross section with those from *BABAR* with $\eta \to \pi^+\pi^-\pi^0$, shown by open circles [11], from the SND experiment with $\eta \to \gamma\gamma$, shown by squares [33], and with those from the CMD-3 experiment, also based on $\eta \to \gamma\gamma$, shown by triangles [34]. The insert shows an expanded view of the resonant region.

to model the signal and a polynomial to model the background. The BW function is convolved with a Gaussian distribution that accounts for the detector resolution. The result of the fit is shown in Fig. 20(a). We obtain 2808 ± 180 $\omega 3\pi^0$ events. The number of $\omega 3\pi^0$ events as a function of the six-pion invariant mass is determined by performing an analogous fit of events in Fig. 12(c) in each 0.05 GeV/c^2 interval of $m(\pi^+\pi^-4\pi^0)$. The resulting distribution is shown in Fig. 20(b).

For the $e^+e^- \to \omega 3\pi^0$ channel, there can be a peaking background from $e^+e^- \to \omega 2\pi^0$ when the fourth π^0 is formed from background photons. A simulation of this reaction with proper normalization leads to the peaking background estimation, which is found to be small as shown in Fig. 20(b). There is also a small peaking background from the generic uds reaction. Finally, we need to remove events with correlated ω and η production in the $\omega\eta$ final state, described in Sec. VI G and shown in Fig. 20(b). These contributions are subtracted from the $\omega 3\pi^0$ signal candidate distribution.

The $e^+e^- \to \omega 3\pi^0$ cross section, not associated with $\eta\omega$ and corrected for the $\omega \to \pi^+\pi^-\pi^0$ branching fraction, is shown in Fig. 21 and summarized in Table V. The uncertainties are statistical only. The systematic uncertainties are about 12%. No previous measurement exists for this process. The cross section exhibits a rise at threshold, a decrease at large $E_{\rm c.m.}$ with a signal from J/ψ, and a possible resonance activity around 1.7–2.0 GeV.

I. The $\rho(770)^{\pm}\pi^{\mp}3\pi^0$ intermediate state

A similar approach is followed to study events with a $\rho^{\pm}$ meson in the intermediate state. Because the ρ meson is broad, a BW function is used to describe the signal shape. There are eight $\rho^{\pm}$ candidates per event, leading to a large combinatoric background. To extract the contribution of the $\rho^{\pm}\pi^{\mp}3\pi^0$ intermediate state we fit the events in Fig. 13(a) with a BW function to describe the signal and a polynomial

TABLE IV. Summary of the $e^+e^- \to \eta\omega$ cross section measurement. The uncertainties are statistical only.

$E_{\rm c.m.}$ (GeV)	σ (nb)	$E_{\rm c.m.}$ (GeV)	σ (nb)	$E_{\rm c.m.}$ (GeV)	σ (nb)	$E_{\rm c.m.}$ (GeV)	σ (nb)	$E_{\rm c.m.}$ (GeV)	σ (nb)
1.425	0.11 ± 0.22	2.075	0.14 ± 0.15	2.725	0.05 ± 0.04	3.375	0.08 ± 0.08	4.025	0.00 ± 0.03
1.475	0.27 ± 0.22	2.125	0.12 ± 0.11	2.775	0.09 ± 0.05	3.425	0.03 ± 0.05	4.075	0.02 ± 0.04
1.525	0.42 ± 0.31	2.175	0.18 ± 0.12	2.825	0.07 ± 0.05	3.475	0.04 ± 0.03	4.125	0.05 ± 0.02
1.575	1.24 ± 0.36	2.225	0.00 ± 0.08	2.875	0.07 ± 0.05	3.525	0.08 ± 0.05	4.175	0.00 ± 0.04
1.625	2.16 ± 0.40	2.275	0.12 ± 0.09	2.925	0.09 ± 0.06	3.575	0.00 ± 0.03	4.225	0.00 ± 0.02
1.675	1.98 ± 0.40	2.325	0.06 ± 0.07	2.975	0.09 ± 0.06	3.625	0.04 ± 0.03	4.275	0.01 ± 0.03
1.725	1.06 ± 0.34	2.375	0.13 ± 0.09	3.025	0.05 ± 0.06	3.675	0.04 ± 0.03	4.325	0.00 ± 0.04
1.775	0.33 ± 0.28	2.425	0.12 ± 0.07	3.075	0.38 ± 0.10	3.725	0.00 ± 0.04	4.375	0.01 ± 0.01
1.825	0.62 ± 0.28	2.475	0.14 ± 0.08	3.125	0.21 ± 0.08	3.775	0.04 ± 0.03	4.425	0.00 ± 0.03
1.875	0.28 ± 0.22	2.525	0.13 ± 0.08	3.175	0.07 ± 0.06	3.825	0.01 ± 0.02	4.475	0.00 ± 0.03
1.925	0.10 ± 0.24	2.575	0.10 ± 0.05	3.225	0.11 ± 0.04	3.875	0.03 ± 0.03		
1.975	0.31 ± 0.19	2.625	0.15 ± 0.07	3.275	0.04 ± 0.04	3.925	0.03 ± 0.02		
2.025	0.46 ± 0.19	2.675	0.08 ± 0.05	3.325	0.05 ± 0.08	3.975	0.03 ± 0.02		

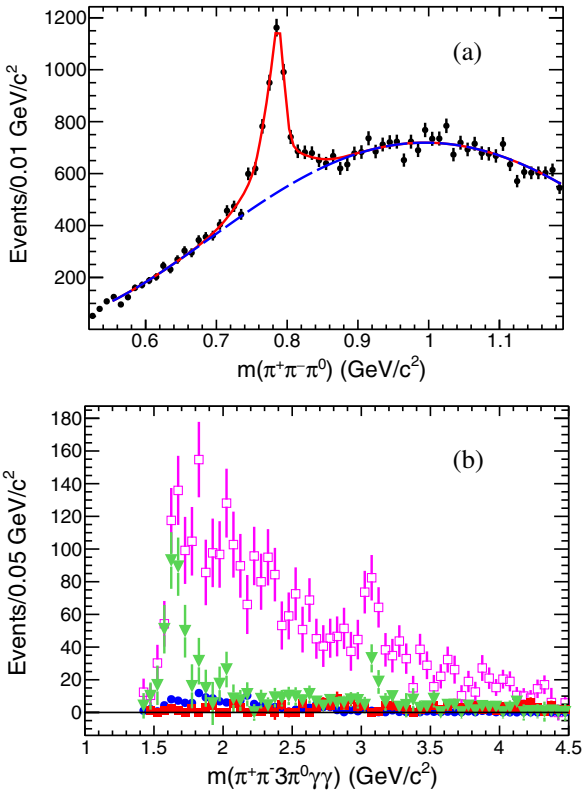

FIG. 20. (a) The $\pi^+\pi^-\pi^0$ invariant mass for data. The solid curve shows the fit function for signal (based on a fit to MC simulation) plus the polynomial for the combinatorial background (dashed curve). (b) The mass distribution of the $\pi^+\pi^-4\pi^0$ events in the ω peak (open squares) and the estimated contribution for $\omega\eta$ (triangles), $\omega 2\pi^0$ (circles), and *uds* (filled squares).

to describe the background. The parameters of the ρ resonance are taken from Ref. [29]. The result of the fit is shown in Fig. 22(a). We obtain 5965 ± 667 combinations with $\rho^{\pm}$ signals. The distribution of these events vs the six-pion invariant mass is shown by the triangle symbols in Fig. 22(b), while a similar fit for the *uds* simulation is shown by squares. The *uds* background dominates at higher energies.

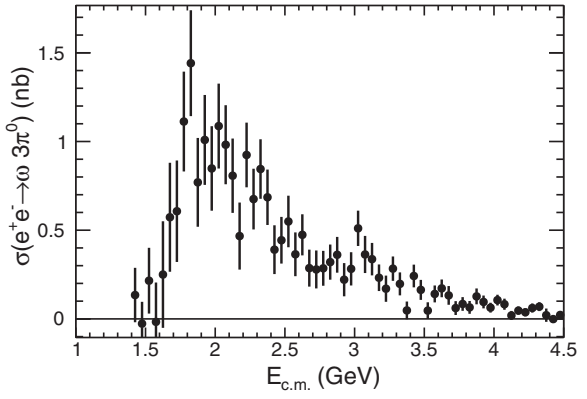

FIG. 21. The energy-dependent $e^+e^- \to \omega 3\pi^0$ cross section in the $\pi^+\pi^-4\pi^0$ mode.

We expect more than one $\rho^{\pm}$ per event, namely that there is a significant production of $e^+e^- \to \rho^+\rho^-2\pi^0$. Because of the large combinatoric background, we do not perform a study of correlated $\rho^+\rho^-$ production.

A similar study of the $\rho^0 4\pi^0$ final state yields 407 ± 45 events in total, but obtained mass dependence is not reliable for this contribution.

J. The sum of intermediate states

The circle symbols in Fig. 23 show the total number of $\pi^+\pi^-4\pi^0$ events, already shown in Fig. 8. We perform a sum of the number of $\eta\pi^+\pi^-\pi^0$, $\omega 3\pi^0$, $\eta\omega$, *uds*, and $\rho^{\pm}\pi^{\mp}3\pi^0$ intermediate-state candidates, found as described in the previous sections, and we show this sum by the square symbols in Fig. 23. This summed curve is seen to be in agreement with the total number of $\pi^+\pi^-4\pi^0$ events except in the region above 2.5 GeV, where the sum is dominated by the $\rho^{\pm}$ signal extraction. The observed overcount indicates a possible contribution from correlated $\rho^+\rho^-$ production.

VII. THE $\pi^+\pi^-3\pi^0\eta$ FINAL STATE

A. Determination of the number of events

An analogous approach to that described above for $e^+e^- \to \pi^+\pi^-4\pi^0$ events is used to study $e^+e^- \to \pi^+\pi^-3\pi^0\eta$ events. We fit the η signal in the fourth-photon-pair invariant mass distribution [cf. Fig. 7(b)] to the sum of two Gaussians with a common mean, while the relatively smooth background is described by a second-order polynomial function, as shown in Fig. 24(a). We obtain 870 ± 52 events. Figure 24(b) shows the mass distribution of these events.

B. Peaking background

The major background producing an η peak is the non-ISR background, in particular $e^+e^- \to \pi^+\pi^-4\pi^0\eta$ in which one of the neutral pions decays asymmetrically, producing a photon interpreted as ISR. The η peak from the *uds* simulation is visible in Fig. 9. We fit the η peak in the *uds* simulation in intervals of 0.05 GeV/c^2 in $m(\pi^+\pi^-3\pi^0\gamma\gamma)$.

To normalize the *uds* simulation, we form the diphoton invariant mass distribution of the ISR candidate with all the remaining photons in the event. Comparing the number of events in the π^0 peaks in data and *uds* simulation, we assign a scale factor of 1.5 ± 0.2 to the simulation. The results are shown by the squares in Fig. 24(b). We subtract these events from the data distribution.

C. Cross section for $e^+e^- \to \pi^+\pi^-3\pi^0\eta$

The cross section for $e^+e^- \to \pi^+\pi^-3\pi^0\eta$ is determined using Eq. (1). We assume the same detection efficiency for

TABLE V. Summary of the $e^+e^- \to \omega\pi^0\pi^0\pi^0$ cross section measurement. The uncertainties are statistical only.

$E_{\text{c.m.}}$ (GeV)	σ (nb)	$E_{\text{c.m.}}$ (GeV)	σ (nb)	$E_{\text{c.m.}}$ (GeV)	σ (nb)	$E_{\text{c.m.}}$ (GeV)	σ (nb)	$E_{\text{c.m.}}$ (GeV)	σ (nb)
1.425	0.13 ± 0.15	2.075	0.98 ± 0.22	2.725	0.28 ± 0.11	3.375	0.05 ± 0.05	4.025	0.11 ± 0.03
1.475	-0.03 ± 0.12	2.125	0.81 ± 0.21	2.775	0.29 ± 0.10	3.425	0.24 ± 0.06	4.075	0.08 ± 0.03
1.525	0.22 ± 0.19	2.175	0.47 ± 0.19	2.825	0.32 ± 0.10	3.475	0.16 ± 0.06	4.125	0.02 ± 0.03
1.575	-0.02 ± 0.22	2.225	0.92 ± 0.18	2.875	0.36 ± 0.10	3.525	0.05 ± 0.05	4.175	0.05 ± 0.02
1.625	0.25 ± 0.30	2.275	0.68 ± 0.17	2.925	0.22 ± 0.09	3.575	0.14 ± 0.05	4.225	0.04 ± 0.02
1.675	0.57 ± 0.31	2.325	0.84 ± 0.17	2.975	0.28 ± 0.09	3.625	0.17 ± 0.05	4.275	0.06 ± 0.03
1.725	0.61 ± 0.29	2.375	0.69 ± 0.16	3.025	0.51 ± 0.10	3.675	0.13 ± 0.05	4.325	0.07 ± 0.02
1.775	1.11 ± 0.28	2.425	0.39 ± 0.14	3.075	0.36 ± 0.10	3.725	0.06 ± 0.04	4.375	0.02 ± 0.04
1.825	1.44 ± 0.30	2.475	0.44 ± 0.13	3.125	0.34 ± 0.09	3.775	0.08 ± 0.04	4.425	0.00 ± 0.02
1.875	0.77 ± 0.25	2.525	0.55 ± 0.15	3.175	0.23 ± 0.07	3.825	0.06 ± 0.04	4.475	0.02 ± 0.01
1.925	1.01 ± 0.25	2.575	0.36 ± 0.12	3.225	0.17 ± 0.07	3.875	0.13 ± 0.04		
1.975	0.85 ± 0.24	2.625	0.47 ± 0.12	3.275	0.28 ± 0.07	3.925	0.10 ± 0.04		
2.025	1.09 ± 0.24	2.675	0.29 ± 0.10	3.325	0.20 ± 0.06	3.975	0.06 ± 0.03		

the photons from the $\pi^0 \to \gamma\gamma$ and $\eta \to \gamma\gamma$ decays. The results are shown in Fig. 25 and listed in Table VI. These are the first results for this process. The systematic uncertainties and corrections are the same as those presented in Table II except that the uncertainty in the detection efficiency increases to 15%.

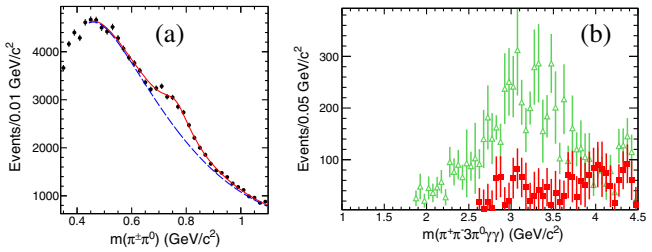

FIG. 22. (a) The $\pi^{\pm}\pi^0$ invariant mass for data. The dashed curve shows the fit to the combinatorial background. The solid curve is the sum of the background curve and the BW function for the $\rho^{\pm}$. (b) The result of the ρ fit in bins of 0.05 GeV/c^2 in the $\pi^+\pi^-3\pi^0\gamma\gamma$ mass. The squares show the contribution from *uds* background.

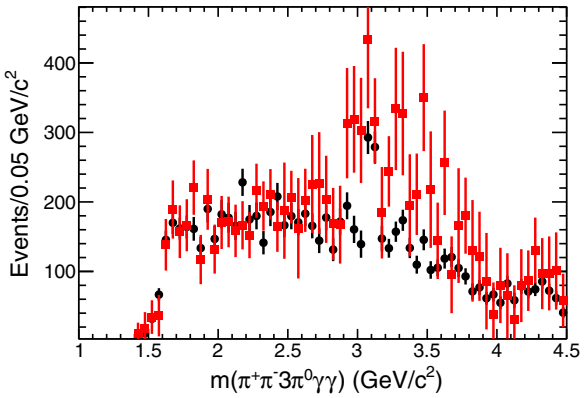

FIG. 23. The circles show the number of events determined from the π^0 fit. The squares show the sum of the number of events with an η, ω, ρ, or *uds* contribution.

The cross section is sizable above 2 GeV. Since this is above the energy range where the final states are summed for the $(g_\mu - 2)$ value calculation, we do not attempt to study the intermediate channels.

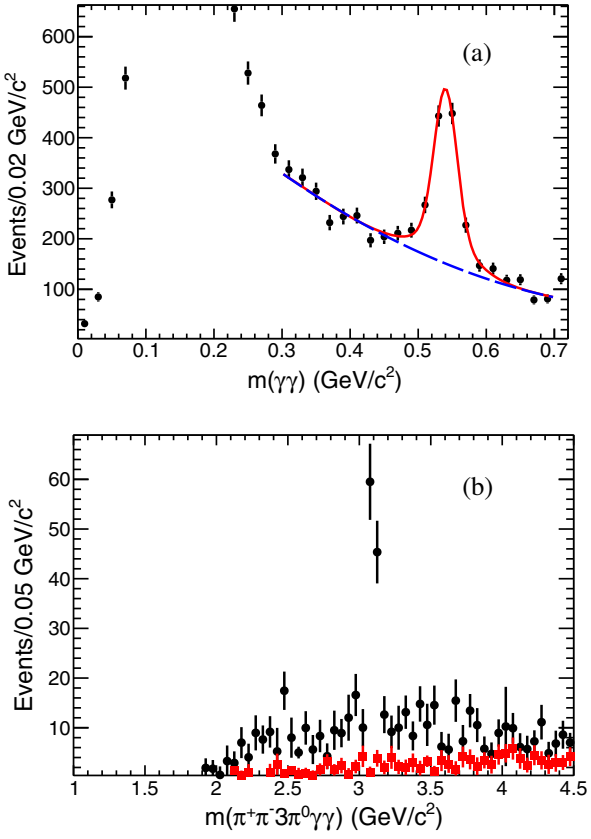

FIG. 24. (a) The expanded view of Fig. 7(b). The solid curve shows the sum of background and the two-Gaussian fit function used to obtain the number of events with an η. (b) The invariant mass distribution for the $\pi^+\pi^-3\pi^0\eta$ events obtained from the η signal fit. The contribution of the *uds* background events is shown by the squares.

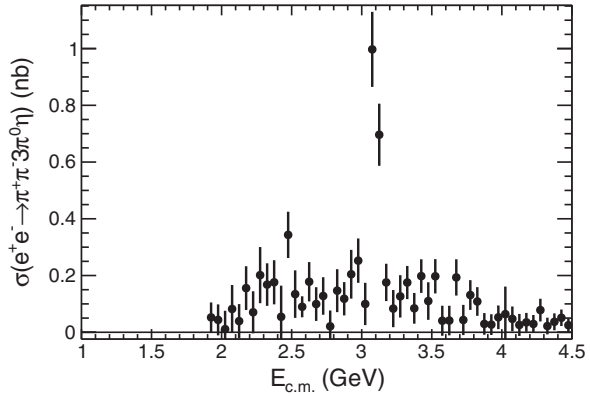

FIG. 25. The energy-dependent cross section for $e^+e^- \to \pi^+\pi^-3\pi^0\eta$. The uncertainties are statistical only.

VIII. THE J/ψ REGION

A. The $\pi^+\pi^-4\pi^0$ final state

Figure 26(a) shows an expanded view of the J/ψ mass region from Fig. 8 for the six-pion data sample. Signals from $J/\psi \to \pi^+\pi^-4\pi^0$ and $\psi(2S) \to \pi^+\pi^-4\pi^0$ are seen. The nonresonant background distribution is well described by the second-order polynomial function in this region.

The observed peak shapes are not purely Gaussian because of radiation effects and resolution, as seen in the simulated signal distributions shown in Fig. 26(b). The sum of two Gaussians is used in the fit. We obtain 340 ± 42 J/ψ events and 28 ± 19 $\psi(2S)$ events. Using the results for the number of events, the detection efficiency, and the ISR luminosity, we determine the product

$$B_{J/\psi\to 6\pi}\cdot\Gamma_{ee}^{J/\psi} = \frac{N(J/\psi\to\pi^+\pi^-4\pi^0)\cdot m_{J/\psi}^2}{6\pi^2\cdot d\mathcal{L}/dE\cdot\epsilon^{\rm MC}\cdot\epsilon^{\rm corr}\cdot C} = (35.8\pm 4.4\pm 5.4)\ \text{eV}, \quad (2)$$

where $\Gamma_{ee}^{J/\psi}$ is the electronic width, $d\mathcal{L}/dE = 180\,\text{nb}^{-1}/\text{MeV}$ is the ISR luminosity at the J/ψ mass $m_{J/\psi}$, $\epsilon^{\rm MC} = 0.018 \pm 0.002$ is the detection efficiency from simulation with the corrections $\epsilon^{\rm corr} = 0.85$, discussed in Sec. VI D, and $C = 3.894\times 10^{11}$ nb MeV^2 is a conversion constant [29]. We estimate the systematic uncertainty for this region to be 15%. The subscript "6π" for the branching fraction refers to the $\pi^+\pi^-4\pi^0$ final state exclusively.

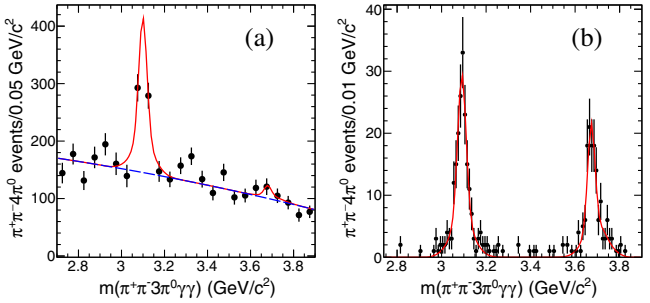

FIG. 26. (a) The $\pi^+\pi^-4\pi^0$ mass distribution for ISR-produced $e^+e^- \to \pi^+\pi^-4\pi^0$ events in the J/ψ–$\psi(2S)$ region. (b) The MC-simulated signals. The J/ψ–$\psi(2S)$ signals ratio is arbitrary. The curves show the fit functions described in the text.

Using $\Gamma_{ee}^{J/\psi} = 5.55 \pm 0.14$ keV [29], we obtain $B_{J/\psi\to 6\pi} = (6.5\pm 0.8\pm 1.0)\times 10^{-3}$; no other measurements for this channel exist.

Using Eq. (2) and the result $d\mathcal{L}/dE = 228\ \text{nb}^{-1}/\text{MeV}$ at the $\psi(2S)$ mass, we obtain

$$B_{\psi(2S)\to 6\pi}\cdot\Gamma_{ee}^{\psi(2S)} = (3.3\pm 2.3\pm 0.5)\ \text{eV}.$$

With $\Gamma_{ee}^{\psi(2S)} = 2.34 \pm 0.06$ keV [29] we find $B_{\psi(2S)\to 6\pi} = (1.4\pm 1.0\pm 0.2)\times 10^{-3}$. For this channel also, no previous result exists.

1. The $\eta\pi^+\pi^-\pi^0$, $\eta\omega$ intermediate states

Figure 27(a) shows an expanded view of Fig. 15 with the $\pi^+\pi^-4\pi^0$ mass distribution for events obtained by a fit to the $3\pi^0$ mass distribution to select events with an η. The two-Gaussian fit, implemented as described above, yields 200 ± 16 and < 20 events at 90% C.L. for the J/ψ and $\psi(2S)$, respectively. Using Eq. (2) we obtain

TABLE VI. Summary of the $e^+e^- \to \pi^+\pi^-\pi^0\pi^0\pi^0\eta$ cross section measurement. The uncertainties are statistical only.

$E_{\rm c.m.}$ (GeV)	σ (nb)	$E_{\rm c.m.}$ (GeV)	σ (nb)	$E_{\rm c.m.}$ (GeV)	σ (nb)	$E_{\rm c.m.}$ (GeV)	σ (nb)	$E_{\rm c.m.}$ (GeV)	σ (nb)
1.925	0.05 ± 0.05	2.475	0.34 ± 0.08	3.025	0.10 ± 0.07	3.575	0.04 ± 0.05	4.125	0.03 ± 0.04
1.975	0.04 ± 0.05	2.525	0.13 ± 0.08	3.075	1.00 ± 0.13	3.625	0.04 ± 0.05	4.175	0.04 ± 0.03
2.025	0.01 ± 0.06	2.575	0.09 ± 0.04	3.125	0.70 ± 0.11	3.675	0.19 ± 0.06	4.225	0.03 ± 0.03
2.075	0.08 ± 0.08	2.625	0.18 ± 0.07	3.175	0.18 ± 0.07	3.725	0.04 ± 0.05	4.275	0.08 ± 0.04
2.125	0.04 ± 0.06	2.675	0.10 ± 0.06	3.225	0.08 ± 0.07	3.775	0.13 ± 0.05	4.325	0.02 ± 0.03
2.175	0.16 ± 0.08	2.725	0.13 ± 0.07	3.275	0.13 ± 0.07	3.825	0.11 ± 0.05	4.375	0.04 ± 0.03
2.225	0.07 ± 0.07	2.775	0.02 ± 0.06	3.325	0.18 ± 0.06	3.875	0.03 ± 0.04	4.425	0.05 ± 0.03
2.275	0.20 ± 0.10	2.825	0.15 ± 0.08	3.375	0.08 ± 0.05	3.925	0.03 ± 0.04	4.475	0.02 ± 0.02
2.325	0.17 ± 0.08	2.875	0.12 ± 0.06	3.425	0.20 ± 0.06	3.975	0.05 ± 0.04		
2.375	0.18 ± 0.08	2.925	0.20 ± 0.09	3.475	0.11 ± 0.07	4.025	0.06 ± 0.10		
2.425	0.05 ± 0.11	2.975	0.25 ± 0.08	3.525	0.20 ± 0.06	4.075	0.05 ± 0.04		

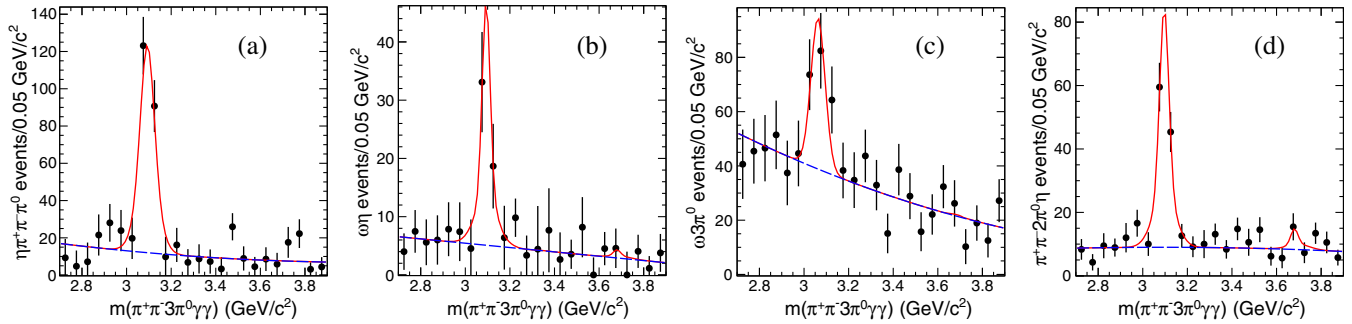

FIG. 27. The J/ψ region for the $\pi^+\pi^-4\pi^0$ events for the selection of (a) $\eta\pi^+\pi^-\pi^0$, (b) $\eta\omega$, (c) $\omega 3\pi^0$, and (d) $\pi^+\pi^-3\pi^0\eta$ intermediate states. The curves show the fit functions described in the text.

$$B_{J/\psi\to\eta\pi^+\pi^-\pi^0}\cdot B_{\eta\to 3\pi^0}\cdot\Gamma_{ee}^{J/\psi} = (21.1\pm 1.7\pm 3.2)\ \text{eV},$$
$$B_{\psi(2S)\to\eta\pi^+\pi^-\pi^0}\cdot B_{\eta\to 3\pi^0}\cdot\Gamma_{ee}^{\psi(2S)} < 3\ \text{eV}.$$

Using $B_{\eta\to 3\pi^0} = 0.3268$ and the value of Γ_{ee} from Ref. [29], we obtain $B_{J/\psi\to\eta\pi^+\pi^-\pi^0} = (11.9\pm 0.9\pm 2.3)\times 10^{-3}$ and $B_{\psi(2S)\to\eta\pi^+\pi^-\pi^0} < 3.5\times 10^{-3}$ at 90% C.L. There are no other measurements of these decays.

Similarly, the expanded view of Fig. 18 is shown in Fig. 27(b) for the subsample of $\pi^+\pi^-4\pi^0$ events with $\eta\to 3\pi^0$ and an additional signal from $\omega\to\pi^+\pi^-\pi^0$. The fit yields 47 ± 20 events corresponding to

$$B_{J/\psi\to\eta\omega}\cdot B_{\eta\to 3\pi^0}\cdot B_{\omega\to\pi^+\pi^-\pi^0}\cdot\Gamma_{ee}^{J/\psi} = (4.9\pm 2.1\pm 0.7)\ \text{eV},$$

which yields $B_{J/\psi\to\eta\omega} = (3.0\pm 1.3\pm 0.5)\times 10^{-3}$, compatible with the current world average result $B_{J/\psi\to\eta\omega} = (1.74\pm 0.20)\times 10^{-3}$ [29].

We can set only an upper limit for the $\psi(2S)\to\eta\omega$ decay: we observe < 20 events corresponding to $B_{\psi(2S)\to\eta\omega} < 14\times 10^{-4}$ at 90% C.L., consistent with the world average value $< 1.1\times 10^{-5}$ [29].

2. The $\omega 3\pi^0$ intermediate state

The expanded view of Fig. 20(b) is shown in Fig. 27(c). The fit yields 89 ± 22 for the $J/\psi\to\omega 3\pi^0$ events corresponding to

$$B_{J/\psi\to\omega 3\pi^0)}\cdot B_{\omega\to\pi^+\pi^-\pi^0}\cdot\Gamma_{ee}^{J/\psi} = (9.4\pm 2.3\pm 1.5)\ \text{eV},$$
$$B_{J/\psi\to\omega 3\pi^0} = (1.9\pm 0.5\pm 0.3)\times 10^{-3}.$$

We use $B_{\omega\to\pi^+\pi^-\pi^0} = 0.892$ from Ref. [29]. No other measurements are available for this decay mode.

We can set only an upper limit for the $\psi(2S)\to\omega 3\pi^0$ decay: we observe < 14 events corresponding to $B_{\psi(2S)\to\omega 3\pi^0} < 8\times 10^{-4}$ at 90% C.L. which is the only measured limit for this decay.

TABLE VII. Summary of the J/ψ and $\psi(2S)$ branching fractions.

		J/ψ or $\psi(2S)$ branching fraction (10^{-3})	
Measured quantity	Measured value (eV)	Derived, this work	PDG [29]
$\Gamma_{ee}^{J/\psi}\cdot B_{J/\psi\to\pi^+\pi^-\pi^0\pi^0\pi^0\pi^0}$	$35.8\pm 4.4\pm 5.4$	$6.5\pm 0.8\pm 1.0$	No entry
$\Gamma_{ee}^{J/\psi}\cdot B_{J/\psi\to\eta\pi^+\pi^-\pi^0}\cdot B_{\eta\to\pi^0\pi^0\pi^0}$	$21.1\pm 1.7\pm 3.2$	$11.9\pm 0.9\pm 2.3$	No entry
$\Gamma_{ee}^{J/\psi}\cdot B_{J/\psi\to\omega\eta}\cdot B_{\omega\to\pi^+\pi^-\pi^0}\cdot B_{\eta\to\pi^0\pi^0\pi^0}$	$4.9\pm 2.1\pm 0.7$	$3.0\pm 1.3\pm 0.5$	1.74 ± 0.20
$\Gamma_{ee}^{J/\psi}\cdot B_{J/\psi\to\omega\pi^0\pi^0\pi^0}\cdot B_{\omega\to\pi^+\pi^-\pi^0}$	$9.4\pm 2.3\pm 1.5$	$1.9\pm 0.5\pm 0.3$	No entry
$\Gamma_{ee}^{J/\psi}\cdot B_{J/\psi\to\pi^+\pi^-\pi^0\pi^0\pi^0\eta}\cdot B_{\eta\to\gamma\gamma}$	$10.6\pm 1.6\pm 1.6$	$4.9\pm 0.8\pm 0.8$	No entry
$\Gamma_{ee}^{\psi(2S)}\cdot B_{\psi(2S)\to\pi^+\pi^-\pi^0\pi^0\pi^0\pi^0}$	$3.3\pm 2.3\pm 0.5$	$1.4\pm 1.0\pm 0.2$	No entry
$\Gamma_{ee}^{\psi(2S)}\cdot B_{\psi(2S)\to\eta\pi^+\pi^-\pi^0}\cdot B_{\eta\to\pi^0\pi^0\pi^0}$	< 3.0 at 90% C.L.	< 3.5 at 90% C.L.	No entry
$\Gamma_{ee}^{\psi(2S)}\cdot B_{\psi(2S)\to\omega\eta}\cdot B_{\omega\to\pi^+\pi^-\pi^0}\cdot B_{\eta\to\pi^0\pi^0\pi^0}$	< 1.1 at 90% C.L.	< 1.4 at 90% C.L.	< 0.11 at 90% C.L.
$\Gamma_{ee}^{\psi(2S)}\cdot B_{\psi(2S)\to\omega\pi^0\pi^0\pi^0}\cdot B_{\omega\to\pi^+\pi^-\pi^0}$	< 1.6 at 90% C.L.	< 0.8 at 90% C.L.	No entry
$\Gamma_{ee}^{\psi(2S)}\cdot B_{\psi(2S)\to\pi^+\pi^-\pi^0\pi^0\pi^0\eta}\cdot B_{\eta\to\gamma\gamma}$	< 1.9 at 90% C.L.	< 2.0 at 90% C.L.	No entry

B. The $\pi^+\pi^-3\pi^0\eta$ final state

The expanded view of Fig. 24(b) is shown in Fig. 27(d). The fit yields 101 ± 16 for the $J/\psi \to \pi^+\pi^-3\pi^0\eta$ events corresponding to

$$B_{J/\psi\to\pi^+\pi^-3\pi^0\eta} \cdot B_{\eta\to\gamma\gamma} \cdot \Gamma_{ee}^{J/\psi} = (10.6 \pm 1.6 \pm 1.6)\ \text{eV},$$
$$B_{J/\psi\to\pi^+\pi^-3\pi^0\eta} = (4.9 \pm 0.8 \pm 0.8) \times 10^{-3}.$$

We set an upper limit for the $\psi(2S) \to \pi^+\pi^-3\pi^0\eta$ decay: we observe < 16 events at 90% C.L. corresponding to $B_{\psi(2S)\to\pi^+\pi^-3\pi^0\eta} < 2.0 \times 10^{-3}$. There are no previous results for this final state.

C. Summary of the charmonium region study

The rates of J/ψ and $\psi(2S)$ decays to $\pi^+\pi^-4\pi^0$, $\pi^+\pi^-3\pi^0\eta$, and several intermediate final states have been measured. The measured products and calculated branching fractions are summarized in Table VII together with the available Particle Data Group [29] values for comparison. Most of the measurements are performed for the first time.

IX. SUMMARY

The excellent photon-energy and charged-particle momentum resolutions, as well as the particle identification capabilities of the *BABAR* detector, allow the reconstruction of the $\pi^+\pi^-4\pi^0$ and $\pi^+\pi^-3\pi^0\eta$ final states produced at center-of-mass energies below 4.5 GeV via initial-state radiation in data collected at the $\Upsilon(4S)$ mass region.

The cross sections for the $e^+e^- \to \pi^+\pi^-4\pi^0$ and the $e^+e^- \to \pi^+\pi^-3\pi^0\eta$ reactions have been measured for the first time. The accuracies are 12% and 15%, respectively.

The selected multihadronic final states in the broad range of accessible energies provide new information on hadron spectroscopy. The observed $e^+e^- \to \omega 3\pi^0$, $e^+e^- \to \eta\pi^+\pi^-\pi^0$, and $e^+e^- \to \eta\omega$ cross sections provide additional information for the hadronic contribution calculation of the muon $g_\mu - 2$.

The initial-state radiation events allow a study of J/ψ and $\psi(2S)$ production and a measurement of the corresponding products of the decay branching fractions and e^+e^- width for most of the studied channels, the majority of them for the first time.

ACKNOWLEDGMENTS

We are grateful for the extraordinary contributions of our PEP-II2 colleagues in achieving the excellent luminosity and machine conditions that have made this work possible. The success of this project also relies critically on the expertise and dedication of the computing organizations that support *BABAR*. The collaborating institutions wish to thank SLAC for its support and the kind hospitality extended to them. This work is supported by the U.S. Department of Energy and National Science Foundation, the Natural Sciences and Engineering Research Council (Canada), the Commissariat à l'Energie Atomique and Institut National de Physique Nucléaire et de Physique des Particules (France), the Bundesministerium für Bildung und Forschung and Deutsche Forschungsgemeinschaft (Germany), the Istituto Nazionale di Fisica Nucleare (Italy), the Foundation for Fundamental Research on Matter (The Netherlands), the Research Council of Norway, the Ministry of Education and Science of the Russian Federation, Ministerio de Economía y Competitividad (Spain), the Science and Technology Facilities Council (United Kingdom), and the Binational Science Foundation (U.S.-Israel). Individuals have received support from the Marie-Curie IEF program (European Union) and the A. P. Sloan Foundation (U.S.).

[1] M. Davier, A. Hoecker, B. Malaescu, and Z. Zhang, Eur. Phys. J. C **77**, 827 (2017); F. Jegerlehner, EPJ Web Conf. **166**, 00022 (2018); A. Keshavarzi, D. Nomura, and T. Teubner, Phys. Rev. D **97**, 114025 (2018).
[2] T. Aoyama *et al.*, Phys. Rep. **887**, 1 (2020).
[3] B. Abi *et al.*, Phys. Rev. Lett. **126**, 141801 (2021).
[4] V. N. Baier and V. S. Fadin, Phys. Lett. **27B**, 223 (1968).
[5] A. B. Arbuzov *et al.*, J. High Energy Phys. 12 (1998) 009.
[6] S. Binner, J. H. Kühn, and K. Melnikov, Phys. Lett. B **459**, 279 (1999).
[7] M. Benayoun *et al.*, Mod. Phys. Lett. A **14**, 2605 (1999).
[8] B. Aubert *et al.* (*BABAR* Collaboration), Phys. Rev. D **69**, 011103 (2004).
[9] B. Aubert *et al.* (*BABAR* Collaboration), Phys. Rev. D **70**, 072004 (2004).
[10] B. Aubert *et al.* (*BABAR* Collaboration), Phys. Rev. D **71**, 052001 (2005).
[11] B. Aubert *et al.* (*BABAR* Collaboration), Phys. Rev. D **73**, 052003 (2006).
[12] B. Aubert *et al.* (*BABAR* Collaboration), Phys. Rev. D **76**, 092005 (2007).
[13] B. Aubert *et al.* (*BABAR* Collaboration), Phys. Rev. D **77**, 092002 (2008).
[14] B. Aubert *et al.* (*BABAR* Collaboration), Phys. Rev. Lett. **103**, 231801 (2009); J. P. Lees *et al.* (*BABAR* Collaboration), Phys. Rev. D **86**, 032013 (2012).

[15] B. Aubert *et al.* (*BABAR* Collaboration), Phys. Rev. D **86**, 012008 (2012).
[16] J. P. Lees *et al.* (*BABAR* Collaboration), Phys. Rev. D **88**, 032013 (2013).
[17] J. P. Lees *et al.* (*BABAR* Collaboration), Phys. Rev. D **88**, 072009 (2013).
[18] J. P. Lees *et al.* (*BABAR* Collaboration), Phys. Rev. D **89**, 092002 (2014).
[19] J. P. Lees *et al.* (*BABAR* Collaboration), Phys. Rev. D **96**, 092007 (2017).
[20] J. P. Lees *et al.* (*BABAR* Collaboration), Phys. Rev. D **98**, 112015 (2018).
[21] J. P. Lees *et al.* (*BABAR* Collaboration), Phys. Rev. D **97**, 052007 (2018).
[22] J. P. Lees *et al.* (*BABAR* Collaboration), Phys. Rev. D **103**, 092001 (2021).
[23] J. P. Lees *et al.* (*BABAR* Collaboration), Nucl. Instrum. Methods Phys. Res., Sect. A **726**, 203 (2013).
[24] B. Aubert *et al.* (*BABAR* Collaboration), Nucl. Instrum. Methods Phys. Res., Sect. A **479**, 1 (2002); **729**, 615 (2013).
[25] H. Czyż and J. H. Kühn, Eur. Phys. J. C **18**, 497 (2001).
[26] A. B. Arbuzov *et al.*, J. High Energy Phys. 10 (1997) 001.
[27] M. Caffo, H. Czyż, and E. Remiddi, Nuovo Cimento A **110**, 515 (1997); Phys. Lett. B **327**, 369 (1994).
[28] E. Barberio, B. van Eijk, and Z. Was, Comput. Phys. Commun. **66**, 115 (1991).
[29] P. A. Zyla *et al.* (Particle Data Group), Prog. Theor. Exp. Phys. (**2020**), 083C01.
[30] S. Agostinelli *et al.* (GEANT4 Collaboration), Nucl. Instrum. Methods Phys. Res., Sect. A **506**, 250 (2003).
[31] T. Sjöstrand, Comput. Phys. Commun. **82**, 74 (1994).
[32] S. Jadach and Z. Was, Comput. Phys. Commun. **85**, 453 (1995).
[33] M. N. Achasov *et al.* (SND Collaboration), Phys. Rev. D **99**, 112004 (2019).
[34] R. R. Ahmetshin *et al.* (CMD-3 Collaboration), Phys. Lett. B **773**, 150 (2017).